



OLLSCOIL NA GAILLIMHÉ

UNIVERSITY OF GALWAY

Investigating the Effect of Ground Layer Adaptive Optics on Speckle Interferometry through Computational Simulations

Thesis by

Shane Foy

In Partial Fulfilment of the Requirements for the

Degree of

Master of Science

Under the supervision of

Dr Nicholas Devaney

School of Natural Sciences

Professor Grace McCormack (Head of the School)

College of Science and Engineering

University of Galway

September 2025

Contents

Contents	i
List of Figures.....	ii
List of Tables.....	v
Acknowledgements	vi
Abstract.....	vii
Chapter 1 Introduction	1
1.1 Background.....	1
1.1.1 Principles of Speckle Interferometry	1
1.1.2 Modern Speckle Interferometry	4
1.1.3 Fourier Phase Estimation	5
1.1.4 Adaptive Optics	8
Chapter 2 Methodology	10
2.1 Simulating Atmospheric Conditions	10
2.2 Fitting the Object Spectrum	12
2.3 Photon Limited Conditions.....	13
2.4 Power Spectrum Signal-to-Noise Ratio	15
2.5 Bispectrum Signal-to-Noise Ratio	17
2.6 Fourier Phase Recovery.....	18
2.7 Ground Layer Adaptive Optics System.....	19
2.8 Simulation Set-Up	22
Chapter 3 Results.....	25
3.1 Speckle Image Generation	25
3.2 Power Spectrum Calibration	26
3.3 Autocorrelation Function	31
3.4 Recovery of Binary Star Parameters	32
3.4.1 High Light Conditons.....	32
3.4.2 Photon-Limited Conditions	39
3.4.3 GLAO Results	48
3.4.4 Recovery of Fourier Phase.....	57
Chapter 4 Discussion & Conclusion	61

List of Figures

Figure 1.1: Formation of a speckle image for a binary star [4].....	3
Figure 1.2: Illustration of the triple correlation technique [16].....	6
Figure 1.3 : Schematic showing the principles of AO [22].	8
Figure 2.1: Phase screen generated using AOtools. In this case, the configuration is screen size = 128, D (telescope diameter) = 8 metres, r_0 (Fried Parameter) = 0.2, L0 (outer scale) = 100, λ = 500 nm.	11
Figure 2.2: Illustration of low light level image generation [29].	14
Figure 2.3: Generation of photon limited speckle images. (a) 1000000 photoevents, (b) 100000 photoevents, (c) 10000 photoevents, (d) 1000 photoevents.	15
Figure 2.4: The first six Zernike polynomials generated using AOtools. (a) Piston, (b) Horizontal Tilt, (c) Vertical Tilt, (d) Oblique Astigmatism, (e) Defocus, (f) Astigmatism.	21
Figure 2.5: Zernike breakdown over 1000 Kolmogorov phase screens generating using AOtools.	22
Figure 2.6: Simulated 4m primary mirror and a 0.5m secondary mirror telescope generated using AOtools.	24
Figure 3.1: Speckle images of a binary star system with two million photoevents. (a) diffraction limited, (b) $r_0 = 0.25$ m, (c) $r_0 = 0.20$ m, (d) $r_0 = 0.15$ m. Separation = 0.077 “, orientation = 135°. 25	25
Figure 3.2: Long exposure image of a binary star system. Same configuration as Figure 3.1 (c). 26	26
Figure 3.3: (a) and (c) are diffraction limited PS of a reference star and binary star respectively. (b) and (d) are PS of the reference star and binary star corresponding to a $r_0 = 0.17$ m and $K = 2,000,000$, separation = 0.077 “, orientation = -270°.	27
Figure 3.4: Calibrated object PS ($r_0 = 0.17$ m, $K = 2,000,000$, separation = 0.077 “, orientation = 45°, Intensity ratio = 1).....	28
Figure 3.5: Intensity ratio = 0.1. Same configuration as Figure 3.4.	28
Figure 3.6: show the speckle image of binary stars and resulting power spectrum SNR of the reference star for 1,000,000, 100,000, and 10,000 photoevents. Separation = 0.077 “, orientation = 135°.	30
Figure 3.7: (a) ACF of a PS with the configuration where $K = 100,000$, $\rho = 0.219$ arcseconds, $\theta = 45^\circ$, and $I = 1.0$. (b) 1D cross section of ACF.....	31
Figure 3.8: Power spectrum SNR of a reference star. $K = 1,500,000$. This graph is logarithmically scaled.	32
Figure 3.9: Model PS along with the calibrated PS. $\rho = 0.077$ ”, $\theta = 270^\circ$, $K = 1,500,000$. (a) $I = 1.0$, (b) = 0.1.	33
Figure 3.10: Recovered intensity ratios from the model under high photon condition. $\rho = 0.077$ ”, $\theta = 270^\circ$, $K = 1,500,000$	34

Figure 3.11: Model PS along with the calibrated PS. $\rho = 0.179''$, $\theta = 59.74^\circ$, $K = 1,500,000$. (a) $I = 1.0$, (b) $= 0.1$	35
Figure 3.12: Recovered intensity ratios from the model under high photon condition. $\rho = 0.179''$, $\theta = 59.74^\circ$, $K = 1,500,000$	35
Figure 3.13: Model PS along with the calibrated PS. $\rho = 0.219''$, $\theta = 45^\circ$, $K = 1,500,000$. (a) $I = 1.0$, (b) $= 0.1$	36
Figure 3.14: Recovered intensity ratios from the model under high photon condition. $\rho = 0.219''$, $\theta = 45^\circ$, $K = 1,500,000$	36
Figure 3.15: Model PS along with the calibrated PS. $\rho = 0.258''$, $\theta = 90^\circ$, $K = 1,500,000$. (a) $I = 1.0$, (b) $= 0.1$	37
Figure 3.16: Recovered intensity ratios from the model under high photon condition. $\rho = 0.258''$, $\theta = 90^\circ$, $K = 1,500,000$	38
Figure 3.17: Calibrated PS, $\rho = 0.077''$, $\theta = 270^\circ$, $I = 1.0$, $K = 200,000$	39
Figure 3.18: Power spectrum SNR for a reference star. $K = 200,000$	40
Figure 3.19: Model PS along with the calibrated PS. $\rho = 0.077''$, $\theta = 270^\circ$, $K = 200,000$. (a) $I = 1.0$, (b) $= 0.1$	40
Figure 3.20: Recovered intensity ratios from the model under limited photon condition. $\rho = 0.077''$, $\theta = 270^\circ$, $K = 200,000$. Error bars denote the standard deviation of the recovered intensity ratios over ten independent simulations.	41
Figure 3.21: Calibrated PS, $\rho = 0.077''$, $\theta = 270^\circ$, $I = 1.0$, $K = 25,000$	42
Figure 3.22: Power spectrum SNR for a reference star. $K = 25,000$	42
Figure 3.23: Model PS along with the calibrated PS. $\rho = 0.077''$, $\theta = 270^\circ$, $K = 25,000$. (a) $I = 1.0$, (b) $= 0.1$	43
Figure 3.24: Recovered intensity ratios from the model under limited photon condition. $\rho = 0.077''$, $\theta = 270^\circ$, $K = 25,000$	43
Figure 3.25: Error in intensity ratio for an intensity ratio of one. For all simulations, $K = 25,000$. 46	
Figure 3.26: Comparison of frequency of fringes for different separations in relation to SNR. Each simulation, $K = 100,000$. The SNR is logarithmically scaled. These fringes are a 1D projection of their respective calibrated PS.	47
Figure 3.27: Measured Intensity ratios for when high and low levels of photons detected for the reference star. $\rho = 0.077''$, $\theta = 270^\circ$. Red dot $K = 25,000$, yellow dot $K = 1,000,000$	48
Figure 3.28: (a) Uncorrected speckle image. (b) Corrected speckle. $\rho = 0.077''$, $\theta = 270^\circ$, $I = 1.0$, $K = 100,000$. Fig 2.28 (b) dimensions are 128×128 pixels. This was done to make it easier for the reader to see the binary stars.....	49
Figure 3.29: Visualisation of GLAO on a speckle image. (a) Uncorrected speckle image. (b) Corrected speckle image (up to 120 Zernikes modes were corrected). $\rho = 0.077''$, $\theta = 270^\circ$, $I = 1.0$, $K = 100,000$	49
Figure 3.30: Power spectrum SNR for a reference star. $K = 100,000$. Up to 120 Zernikes modes were removed from the wavefront for the corrected SNR. SNR was logarithmically scaled.	50

Figure 3.31: Recovered intensity ratios from the model under limited photon condition and GLAO corrected conditions. $\rho = 0.077''$, $\theta = 270^\circ$, $K = 50,000$	51
Figure 3.32: Recovered intensity ratios from the model under limited photon condition and GLAO corrected conditions. $\rho = 0.077''$, $\theta = 270^\circ$, $K = 25,000$	52
Figure 3.33: Minimum number of detected photoevents required for successful recovery of each intensity ratio. $\rho = 0.077''$, $\theta = 270^\circ$	53
Figure 3.34: Comparison of a (a) uncorrected PS and (b) GLAO corrected calibrated PS. $\rho = 0.077''$, $\theta = 270^\circ$, $l = 1.0$, $K = 10,000$	54
Figure 3.35: Recovered intensity ratios from the model under limited photon condition and GLAO corrected conditions. $\rho = 0.179''$, $\theta = 59.74^\circ$, $K = 25,000$	55
Figure 3.36: Minimum number of detected photoevents required for successful recovery of each intensity ratio. $\rho = 0.179''$, $\theta = 59.74^\circ$	55
Figure 3.37: Minimum number of detected photoevents required for successful recovery of each intensity ratio. $\rho = 0.219''$, $\theta = 45^\circ$	56
Figure 3.38: Minimum number of detected photoevents required for successful recovery of each intensity ratio. $\rho = 0.258''$, $\theta = 90^\circ$	57
Figure 3.39: Mean bispectrum (a) modulus and (b) phase of binary star speckle images with configuration of $\rho = 0.077''$, $\theta = 270^\circ$, $K = 200,000$. Subplanes used for (a), $u_2 = 0$, $v_2 = 0$. Subplanes used for (b), $u_2 = 0$, $v_2 = 1$. The bispectrum modulus is logarithmically scaled.	58
Figure 3.40: Logarithmic bispectral SNR. Subplanes used $u_2 = 0$, $v_2 = 1$	58

List of Tables

Table 2.1: Input parameters for the phase screen generated by AOtools.	22
Table 3.1: Recovered separation and orientation from the model for simulation 1.1. Error shown the high accuracy of the model.	34
Table 3.2: Recovered separation and orientation from the model for simulation 2.1. Error shown the high accuracy of the model.	35
Table 3.3: Recovered separation and orientation from the model for simulation 3.1. Error shown the high accuracy of the model.	37
Table 3.4: Recovered separation and orientation from the model for simulation 3.1. Error shows the high accuracy of the model.	38
Table 3.5: Error % from recovered intensity ratio for both photon levels. $\rho = 0.077''$, $\theta = 270^\circ$	44
Table 3.6: Recovered intensity ratios for both photon levels. $\rho = 0.179''$, $\theta = 59.74^\circ$	44
Table 3.7: Error % from recovered intensity ratio for both photon levels. $\rho = 0.179''$, $\theta = 59.74^\circ$	44
Table 3.8: Recovered intensity ratios for both photon levels. $\rho = 0.219''$, $\theta = 45^\circ$	45
Table 3.9: Error % from recovered intensity ratio for both photon levels. $\rho = 0.219''$, $\theta = 45^\circ$	45
Table 3.10: Recovered intensity ratios for both photon levels. $\rho = 0.258''$, $\theta = 90^\circ$	45
Table 3.11: Error % from recovered intensity ratio for both photon levels. $\rho = 0.258''$, $\theta = 90^\circ$	46
Table 3.12: Error from cost function for high-light levels, across all simulated intensity ratios. $K = 200,000$, $\rho = 0.077''$	59
Table 3.13: Error from cost function for low-light levels across all simulated intensity ratios. $K = 25,000$, $\rho = 0.077''$	59
Table 3.14: Error from cost function for GLAO conditions, across all simulated intensity ratios. $K = 25,000$, $\rho = 0.077''$. Up to 120 Zernike's was corrected.	60

Acknowledgements

I would like to thank my advisor Dr Nicholas Devaney for all his help in exploring this topic and domain. I would also like to thank my family for all their patience as I pursued this degree.

Abstract

Atmospheric turbulence limits the angular resolution of ground-based telescopes far below the diffraction limit. Speckle interferometry (SI) is a technique that recovers diffraction limited information under the turbulent atmosphere. This thesis investigates the performance of SI for recovering the parameters of binary star systems under photon-limited conditions and assesses the gains achievable with ground-layer adaptive optics (GLAO).

Speckle images of both binary stars and reference stars were generated through numerical simulation, with atmospheric turbulence modelled by Kolmogorov phase screens. Fourier-domain analysis of these images produced the corresponding power spectra, which—after calibration—were used to extract the binary separation, position angle, and intensity ratio, while a least-squares bispectrum algorithm recovered the Fourier phase to resolve the intrinsic 180° orientation ambiguity.

Results show that SI reliably recovers binary parameters at high photon counts. Intensity-ratio estimates become biased and increasingly variable as the number of photoevents decreased to approximately 25,000 photoevents. Incorporating GLAO, modelled via removal of up to 120 Zernike modes from one of two phase screens, significantly improved fringe contrast and reduced the number of photoevents required for reliable recovery of binary parameters by more than an order of magnitude.

These findings demonstrate that combining SI with GLAO correction enables diffraction-limited measurements of binaries at visible wavelengths using relatively low photonevents. The study provides practical thresholds and error estimates for observing faint binaries with 4-m class telescopes and offers a computational framework readily extendable to real observational data and more advanced adaptive-optics configurations.

Chapter 1 Introduction

The performance of a telescope is determined by its resolution capabilities. Due to the wave nature of light, there is a physical limit at which the telescope can perform. The limit, which is called the diffraction limit, is set by the size of the mirror of the telescope. Unfortunately for ground-based telescopes, this limit can never be reached because of the atmosphere. Plane wavefronts of light from stars pass through the atmosphere, these wavefronts become distorted due to inhomogeneities in the atmosphere, resulting in a perturbed wavefront reaching the telescope. The inhomogeneities are caused by varying temperature, densities and wind speed. This thesis investigates two primary techniques to mitigate atmospheric distortion.

Speckle Interferometry (SI) is a technique that involves capturing atmospherically degraded short exposure narrowband images, called speckle images. This results in speckles, which contain diffraction limited information about the object. Using various Fourier-transform techniques, the power spectra are analysed to recover diffraction-limited information.

Adaptive Optics (AO) is a piece of equipment that can be added to the telescope. It uses deformable mirrors that adjust in real-time to correct atmospheric aberrations. The aim of this thesis is to outline in detail the effects of atmospheric turbulence on telescopic performance and how introducing an adaptive optic system improves the telescope's overall performance. This will be done through the techniques above on simulated binary star systems.

1.1 Background

Prior to the 1960s, the imaging of space objects was always done through long exposure images. This was primarily to collect sufficient light from faint objects. Tatarskii [1] contributed significantly to the theoretical understanding of the turbulent atmosphere by integrating Kolmogorov's statistical theory of turbulence with the principles of electromagnetic wave propagation [2]. This new understanding of the turbulent atmosphere led to innovative methods of overcoming atmospheric degradation of images. In the 1970s, Labeyrie [3] recognized that speckles in short exposure images contained higher spatial frequency information about the object than long exposure images. He concluded that the speckles in a short-exposure image are roughly the size of an Airy disk observed without aberrations or atmospheric seeing, so they can be interpreted as a collection of randomly shifted diffraction-limited images, demonstrating the presence of high-spatial-frequency information. Labeyrie conceived the idea of Speckle Interferometry (SI).

1.1.1 Principles of Speckle Interferometry

In this section, imaging theory through the atmosphere, adapted from Kuwamura [4], is detailed, followed by Labeyrie's SI technique.

The image $i(x, y)$ of an object $o(x, y)$ imaged with a telescope is given by the convolution

$$i(x, y) = \iint_{-\infty}^{\infty} o(x', y') h(x' - x, y' - y) dx' dy' \quad (1.1)$$

$$i(x, y) = o(x, y) * h(x, y) \quad (1.2)$$

where $h(x, y)$ is the point spread function (PSF) which describes the image of a point source which has been affected by telescopic and atmospheric aberrations. Due to diffraction, a telescope has a fixed natural limit on its resolution ability. This resolution depends on the size of its Airy disk. For incident light of wavelength λ and telescope diameter D , the angular resolution in radians, is given by

$$\theta = \frac{1.22\lambda}{D} \quad (1.3)$$

For ground-based telescopes, however, theoretical diffraction limited images will never be obtained because of atmospheric degradation of the incoming light waves. Random fluctuations in atmospheric temperature and density create variations in the refractive index, which in turn distort both the phase and amplitude of an incoming plane wavefront. The amplitude fluctuations are known as scintillations (twinkling) while the phase fluctuation is important for imaging purposes and is the major component of this work. Fried [5] was able to quantify the extent of atmospheric turbulence by a parameter later known as the Fried parameter, r_0 , which quantifies wavefront aberration caused by the atmosphere. It is defined as the diameter of a circular region over which the root-mean-square (RMS) wavefront aberration introduced by atmospheric turbulence equals one radian.

The instantaneous image, $i_n(x, y)$, of an object is therefore given by

$$i_n(x, y) = o(x, y) * h_n(x, y) \quad (1.4)$$

where $h_n(x, y)$ instantaneous PSF. Due to the PSF's temporal fluctuation, this convolution produces a speckled image of the object, with the speckles continuously changing. The size of the speckles themselves is proportional to the size of the diffraction-limited Airy disk ($\propto \lambda/D$), whereas the spread of the speckle grains depends on the Fried parameter mentioned above ($\propto \lambda/r_0$). The binary star image in Figure 1.1 serves as an example of this. The perturbed wavefront is depicted as plane wavefronts from a distant binary propagate through the turbulent atmosphere. The speckled image at the focal plane is then produced by the perturbed wavefront propagating through an aperture.

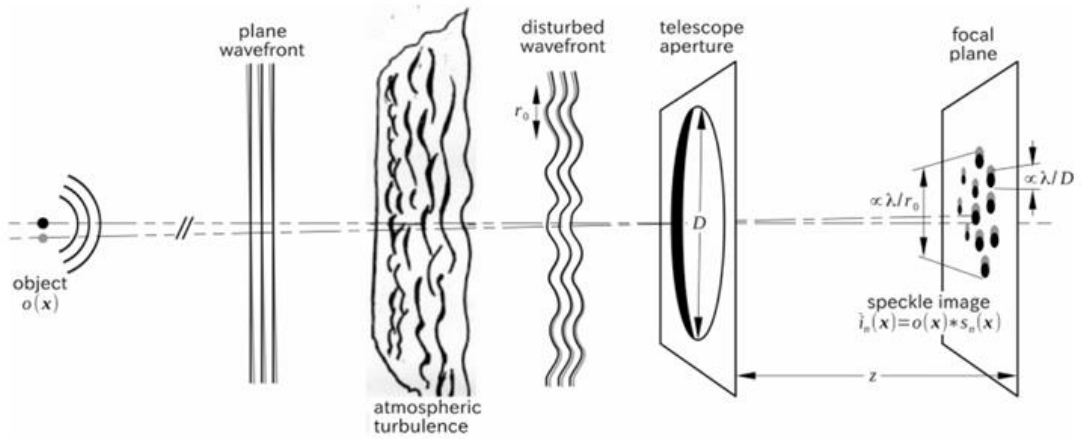


Figure 1.1: Formation of a speckle image for a binary star [4].

According to the Convolution Theorem, taking a Fourier Transform (FT) of the speckled image results in Equation (1.2) becoming a product rather than a convolution

$$I(u, v) = O(u, v)H(u, v) \quad (1.5)$$

where u and v are spatial frequencies, and $I(u, v)$, $O(u, v)$ and $H(u, v)$ are the FT of $i(x, y)$, $o(x, y)$ and $h(x, y)$ respectively. $H(u, v)$ is known as the Optical Transfer Function (OTF) which is complex valued for all frequencies up to the diffraction limit.

Given a set of N short exposure images $i_n(x, y)$ and taking their FT, their ensemble average is given by

$$\langle I_n(u, v) \rangle = O(u, v) \langle H_n(u, v) \rangle \quad (1.6)$$

The action of averaging the short exposure images smooths out the speckles into a 'seeing disk' proportional in size to λ/r_0 , which results in a blurred image of the object and is essentially a long exposure image of the object. This sets the limits of long exposure imagery through a turbulent atmosphere, and for $D > r_0$, will be worse than diffraction-limited resolution.

At this point, Labeyrie's [6] Speckle Interferometry demonstrates its effectiveness. Since averaging N short exposure images suppresses high spatial frequencies, SI can retain high spatial frequency information by taking the squared modulus of the Fourier transformed short exposure images and averaging the power spectrum set:

$$\langle |I_n(u, v)|^2 \rangle = |O(u, v)|^2 \langle |H_n(u, v)|^2 \rangle \quad (1.7)$$

As mentioned above, the speckles are similar in size of the Airy disk and contain diffraction limited information. When a binary star system is observed, the resulting image displays the superposition of the two individual speckle patterns. Applying Equation (1.7), to short exposure images of a binary star system, results in a fringe pattern appearing. From these fringes, information about the system can be gathered. For example, the periodicity of the fringes indicates the separation between the two stars. The binary's position angle and intensity ratio can also be determined.

It can be shown that $\langle |H_n(u, v)|^2 \rangle = \langle H_n(u, v) \rangle^2 + \left(\frac{D}{r_0}\right)^2 T_0(u, v)$, where $\langle H_n(u, v) \rangle^2$ is the low frequency long exposure transfer function, and $T_0(u, v)$ is the diffraction-limited telescope transfer function. The factor $\left(\frac{D}{r_0}\right)^2$ equals the average number of speckles in the short exposure image.

1.1.2 Modern Speckle Interferometry

Since its conception, there have been various methods developed based on the core principles of SI. In the standard technique the idea is to take the averaged power spectrum (PS) over many speckle images and then deconvolve the OTF with an unresolved point star [7]. After this step is done, a fitting is made to gather information about the binary.

There are two types of fittings; one is made in the image domain where measurements are taken from the autocorrelation function (ACF) [8]. The ACF is the inverse FT of the object PS. The ACF function of a binary star system shows a central peak and two lateral peaks with equal intensities. The distance between the central and lateral peaks gives the stars separation. The ACF is a quick and effective way to determine the separation of a binary.

The other fitting is done in the Fourier domain; the object PS shows fringes where a sinusoidal fit can be applied. From this fitting, separation and intensity ratio can be found. One advantage of fitting in the Fourier domain is that it makes it possible to compare the object PS to the known physical model for a double point source's spectrum with relative ease. In recent work, the most common method to get information about the binary is to use a mixture of both; get the separation and orientation from the ACF and the fitting in the Fourier domain gets the intensity ratio [9].

The SI technique presents significant challenges in producing reliable intensity ratio estimates. Measurements of intensity ratios, prior to any correction have previously been assigned uncertainties as large as approximately $\pm 150\%$ [10]. Several factors can lead to errors; one is due to the OTF needing to be deconvolved with a point source, and in reality, the point source star and the test star system can't be observed under the exact same seeing conditions [11]. Another potential error arises if the secondary star's speckle pattern lies outside the primary star's isoplanatic patch—the region where wavefront distortions remain uniform. Because the image frame is centred on the primary star, the secondary speckles may extend beyond the frame, causing a loss of flux from the secondary [12]. The maximum detectable intensity ratio

is highly dependent on the binary separation. The fitting performs poorly for binaries close to the diffraction limit of the telescope but as the separation increases, the performance of the fitting improves [13]. This detection limit increases as the diameter of the telescope increases. The speckle system on the Southern Astrophysical Research (SOAR) 4.1 m and Wisconsin-Indiana-Yale-NOIRLab (WIYN) 3.5 m telescopes can measure intensity ratios up to 40 at 0.2" separation while the Gemini 8.1 m can detect a binary stars with an intensity ratio of 100:1 at 0.1" separation. [13, 14, 11].

There is a caveat to the orientation of the binary system in both techniques; there is an 180° ambiguity in the orientation of the binary system. This is due to the nature of PS. To know exactly the orientation, the phase of the spatial frequency needs to be recovered from the speckle images.

1.1.3 Fourier Phase Estimation

Phase information about the object viewed through a turbulent atmosphere is lost in SI which provides the modulus of the Fourier transform of the object. The phase information is important to eliminate the 180° ambiguity in the fitting of the PS mentioned above. Phase information is essential in image reconstruction. Reconstructing the unknown object phase has been a long-standing focus of extensive research.

Several techniques have been developed to recover the phase. Phase can be recovered in the spatial domain or the Fourier domain. In the spatial domain there is a technique called speckle masking. In speckle masking, the average triple correlation of many short exposure images is calculated via

$$\langle I_n^{(3)}(\mathbf{x}, \mathbf{x}') \rangle = \langle [I_n(\mathbf{x}) \cdot I_n(\mathbf{x} + \mathbf{x}')] \otimes I_n(\mathbf{x}) \rangle \quad (1.8)$$

Equation (1.8) involves computing the average of a triple correlation, constructed by multiplying a speckle interferogram with spatially shifted versions of itself, followed by cross-correlation and ensemble averaging. In the speckle masking approach, the following processing steps are such that the average triple correlation $\langle I_n^{(3)}(\mathbf{x}, \mathbf{x}') \rangle$ of many speckle interferograms yields the diffraction-limited object triple correlation $O_n^{(3)}(\mathbf{x}, \mathbf{x}')$, therefore,

$$\langle I_n^{(3)}(\mathbf{x}, \mathbf{x}') \rangle \rightarrow O_n^{(3)}(\mathbf{x}, \mathbf{x}') \quad (1.9)$$

where \rightarrow denotes the compensation of the speckle transfer function.

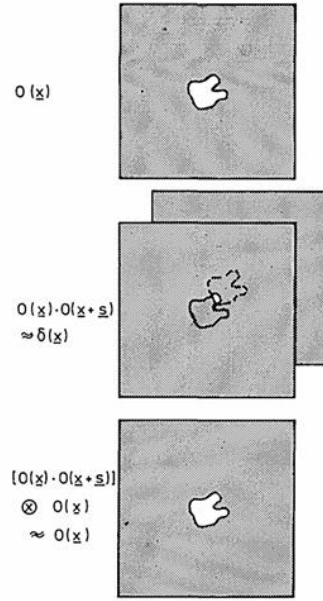


Figure 1.2: Illustration of the triple correlation technique [16].

A straightforward example demonstrating the value of the object triple correlation is shown in Fig. 3. Multiplying the object $O(x)$ by the shifted copy of the object $O(x + s)$ is the first step in the example. The shift vector $x' = s$ is called the masking vector. This vector s is selected such that the product mask $O(x) \cdot O(x + s)$ is approximately a δ function. In this case the cross correlation of the product mask with the object yields

$$[O(x) \cdot O(x + x')] \otimes O(x) \approx O(x) \quad (1.10)$$

Therefore, a true image of the object is contained in a 2-D subplane of the 4-D object triple correlation $O^{(3)}(x, x')$ [16]. Taking the Fourier transform of the triple correlation gives the bispectrum.

The bispectrum is another approach to recover the phase spectrum from short exposure images. The bispectrum uses a specialized moment of the measured image spectrum. The bispectrum of a short exposure image is defined by

$$I^{(3)}(\mathbf{u}, \mathbf{v}) = I(\mathbf{u})I(\mathbf{v})I(-\mathbf{u} - \mathbf{v}) = |I^{(3)}(\mathbf{u}, \mathbf{v})| \exp[i\psi(\mathbf{u}, \mathbf{v})] \quad (1.11)$$

where \mathbf{u} and \mathbf{v} are both 2D spatial frequencies, $\psi(\mathbf{u}, \mathbf{v})$ is the bispectral phase. The bispectrum is a 4D structure and has 8-fold symmetry [15]. The bispectrum is a triple product in four dimensions, to get an understanding of the sheer size of a bispectrum structure, as an example, a 128×128-pixel image generates over 260 million bispectral values—highlighting the scale of data involved. This number arises because, for each frequency point, there are nearly 128^2 combinations of bispectral terms, and that's only for one image, SI typically takes 1000's of images. This requires unrealistic computational power. If $(-\mathbf{u} - \mathbf{v})$ is constrained to a small range, this makes it computationally viable.

Lohmann et al. [16] demonstrated that the bispectra of individual speckle frames can be averaged similarly to the power spectrum, and in the limit of an infinite number of speckle frames

$$\langle S^{(3)}(\mathbf{u}, \mathbf{v}) \rangle = I^{(3)}(\mathbf{u}, \mathbf{v}) \langle H^{(3)}(\mathbf{u}, \mathbf{v}) \rangle \quad (1.12)$$

where $\langle H^{(3)}(\mathbf{u}, \mathbf{v}) \rangle$ is the generalised bispectrum transfer function. Moreover, they showed that $\langle H^{(3)}(\mathbf{u}, \mathbf{v}) \rangle$ is real and non-zero up to the telescope frequency cutoff, a property that is approximately independent of minor telescope aberrations [16]. Therefore, the phase of the object Fourier transform is encoded in the bispectral phase through the relation

$$\psi(\mathbf{u}, \mathbf{v}) = \phi(\mathbf{u}) + \phi(\mathbf{v}) - \phi(\mathbf{u} + \mathbf{v}) \quad (1.13)$$

where $\phi(\mathbf{u})$ is the true object phase.

Recovering the object's Fourier phase from the bispectral phase in Equation (1.13) has been extensively studied. The specific properties of Equation (1.13) make this phase reconstruction feasible. This can be accomplished using least-squares or recursive approaches. Recursive methods [16,17] use the linear combinations of Fourier phases found in each bispectral phase to sequentially deduce the object phases. While recursive methods are computationally efficient, their performance deteriorates at higher spatial frequencies, particularly in noisy data. The least-squares approach tries to simultaneously fit the complete set of object Fourier phase with the bispectral phase in a least-squares sense. Least-squares algorithms have been proved to be the most robust and reliable and outperforms the recursive methods for recovering the object phase especially at high spatial frequencies [18,19]. While there are variations in the least-squares approach, the main idea is to minimize an objective function. The goal is to find the best fit phases to the measured bispectral phase to reduce the error sum. This requires an unwrapping of the bispectrum phase since it is a modulo 2π quantity, which particularly affects the recursive method. An optimisation algorithm is used to find the minimum error of the objective function. Least-squares algorithms have proven to perform effectively in real and simulated data that has been compromised by noise [18]. The recovery

of the object phase can also be done without a reference star, but the image quality is not better than conventional algorithms that uses a reference star, as noted by Glindemann [18].

It should also be noted that Northcott et al. [20] developed a reconstruction technique based on the projection-slice theorem and the Radon transform

1.1.4 Adaptive Optics

Apart from post processing techniques to improve image quality, Adaptive Optics (AO) is a powerful instrument to overcome atmospheric distortions to produce near diffraction limited images. AO was first envisioned in 1953 by Horace W. Babcock [21] but it wasn't viable until the 1980s when advancements in computer technology made the technique possible.

AO is an instrument made up of deformable mirrors and wavefront sensors. As mentioned above light from an astronomical object passes through the atmosphere and gets distorted, the wavefront sensors measure this light, a computer analyses it and calculates the optimal shape of the deformable mirrors to correct the all aberrations induced by the atmosphere, resulting in a much-improved image. This happens on a timescale of a few milliseconds because for that length of time, the atmosphere is essentially frozen, allowing the light to be corrected before the atmosphere changes again.

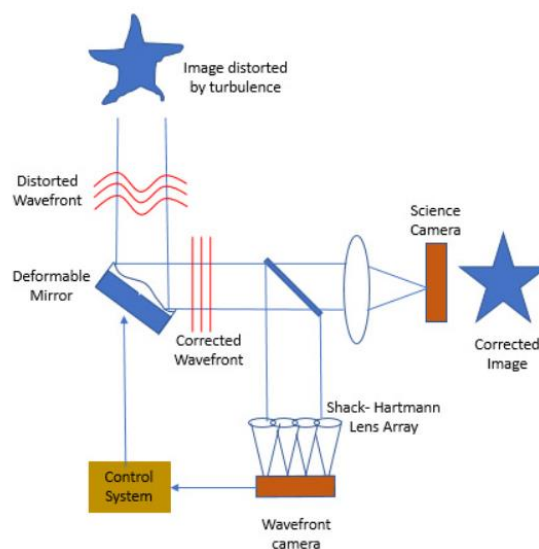


Figure 1.3 : Schematic showing the principles of AO [22].

This type of AO, which will be named classical AO from here on, has been employed on 8m class telescopes. Classical AO on an 8m telescope can produce a >80% Strehl ratio on long exposure near-infrared images [21]. Strehl ratio measures the quality of optical images, specifically the performance of an optical system compared to its diffraction-limited performance. However, classical AO has its drawbacks. Classical AO can only work effectively in the infrared wavelength. This is due to infrared light being less affected by atmospheric

turbulence than visible light, also the isoplanatic angle is larger for infrared light. Classical AO itself can only cover a small percentage of the sky; it can increase its sky coverage with the use of laser guide stars (LGS) [21]. Another approach was developed to increase the field of view (FoV) called ground-layer adaptive optics (GLAO). Proposed by Rigaut [23] in 2002, GLAO doesn't try to get diffraction limited images but rather improves seeing. Tokovinin et al. showed that most of the turbulence is concentrated within a few hundred metres above the ground [24]. GLAO works by correcting the atmospheric turbulence at the pupil to a height of approximately 1km. Distortions caused by the atmosphere at low altitudes are isoplanatic and cover a wide field. These distortions are measured using laser guide stars (LGS). Hart et al. showed in 2010, at the 6.5 m MMT telescope in Arizona, that seeing improved by a factor of 3 when GLAO was used [25]. As noted by Tokovinin "The advantages of increased angular resolution (or energy concentration in an instrument aperture) in a wide field in the visible surpass those of classical AO for many astronomical applications" [26].

GLAO uses several guide stars, and applying an average, will estimate the ground-layer turbulence, which affects the light from all stars in the same way.

Chapter 2 Methodology

2.1 Simulating Atmospheric Conditions

An essential component of this work is the simulation of the atmosphere. Kolmogorov statistics was chosen to model the effect of the atmosphere on incoming light from a binary star system. A detailed explanation of Kolmogorov turbulence model is described in Quirrenbach [27] and Mclean [28], but a brief description is outlined below.

The atmosphere is considered to be a fluid, and its properties are determined by the Reynolds number $R = VL/\nu$, where V is the fluid velocity, L is the characteristic length scale, and ν is viscosity of the fluid. If $R < 100$, the fluid has laminar flow but for the atmosphere, $R \approx 10^6$ and therefore is turbulent.

The atmosphere is divided into cells called eddies with sizes up to a maximum 'outer scale', L_0 . These eddies cascade into smaller eddies down to an 'inner scale', l_0 , where the kinetic energy is dissipated as heat. L_0 values range from tens to hundreds of meters while l_0 are typically on the scale of millimetres [27]. The properties of a turbulent atmosphere are described statistically by its spatial structure function.

Kolmogorov's model of the turbulent atmosphere states that different parts of the atmosphere have different indices of refraction, due mainly to fluctuations in temperature. This causes phase delays in the incoming light. Kolmogorov's model is described by the spatial structure function $D_n(r)$, which gives the difference squared between two refractive indices separated by a distance $r = (r_1 - r_2)$

$$D_n(r) = \langle |n(r_1) - n(r_2)|^2 \rangle = C_n^2 r^{\frac{2}{3}} \quad (2.1)$$

C_n^2 is a measure of strength of the turbulent atmosphere and values range from $10^{-14} \text{ m}^{-2/3}$ to $10^{-15} \text{ m}^{-2/3}$ at the ground level and goes as low as $10^{-18} \text{ m}^{-2/3}$ at 10km above the surface of earth [28].

As mentioned in section 1.1.1, an atmospherically perturbed wavefront has variations in both amplitude and phase, with phase contributing more to image quality. The effects of phase variations caused by a thin turbulent layer, δh , on a wavefront, is determined by deriving the phase structure function and integrating through the atmosphere. The phase structure function for Kolmogorov turbulence is given by

$$D_\phi(r) = 6.88 \left(\frac{r}{r_0} \right)^{\frac{5}{3}} \quad (2.2)$$

where

$$r_0(\lambda, z) = 0.185 \lambda^{\frac{6}{5}} \cos^{\frac{3}{5}} z \left(\int C_n^2 dh \right)^{-\frac{3}{5}} \quad (2.3)$$

or

$$r(\lambda) = \left(\frac{\lambda}{\lambda_0}\right)^{\frac{6}{5}} r_0 \quad (2.4)$$

and λ is the wavelength, and z is zenith distance angle of a star. The Fried parameter, r_0 , is an important quantity because it characterises the size of the eddies, and therefore, determines the quality of seeing conditions.

Kolmogorov Phase Screens are simulated using the AOtools library, as detailed in Townson [29]. The class used to generate the phase screen in figure 2.1 below is `aotools.turbulence.infinitephasescreen.PhaseScreenKolmogorov`, which are based on the examples given in [30]. This method also generates infinite Kolmogorov phase screen described by Assemat and Wilson [31], which uses the Fried method for Kolmogorov turbulence. This technique represents the phase addition light experiences when passing through atmospheric turbulence. To simulate wind driven motion in the atmosphere, this method preserves a small portion of phase and expands it as needed for as many steps as needed, in contrast to other phase screen production techniques that translate a big static screen. This can drastically cut down on memory usage, but it will demand more computing power. This function returns a 2D array with deviations in phase given in radians.

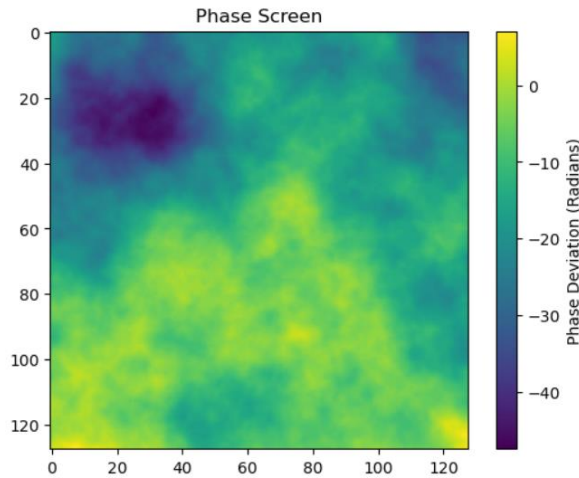


Figure 2.1: Phase screen generated using AOtools. In this case, the configuration is screen size = 128, D (telescope diameter) = 8 metres, r_0 (Fried Parameter) = 0.2, L_0 (outer scale) = 100, λ = 500 nm.

2.2 Fitting the Object Spectrum

The technique for finding an estimate of the object's Fourier modulus was adapted from Kuwamura et al. [4].

PS of the individual short exposure images were taken and averaged over many frames; this results in the image PS defined by Equation (1.7). Binary parameters can be retrieved from the object's Fourier modulus $|O(u, v)|$. To find this, the averaged squared modulation transfer function (MTF) of the system needs to be known. Normally to get this, many short exposure images are taken of an unresolvable star (reference star) shortly before or after measurements on the test object, and that is near the object of interest, so that it can be assumed to be under the same atmospheric conditions as the test object. The reference star acts like a point source, and by computing the ensemble-averaged power spectrum from its frames, the squared modulation transfer function (MTF) of the system can be estimated:

$$\langle |I_n^{ref}(u, v)|^2 \rangle = \langle |H_n(u, v)|^2 \rangle \quad (2.5)$$

the object's Fourier modulus is then obtained by

$$\begin{aligned} |O(u, v)| &= \left[\frac{\langle |I_n(u, v)|^2 \rangle}{\langle |H_n(u, v)|^2 \rangle} \right]^{\frac{1}{2}} \\ &= \left[\frac{\langle |I_n(u, v)|^2 \rangle}{\langle |I_n^{ref}(u, v)|^2 \rangle} \right]^{\frac{1}{2}} \end{aligned} \quad (2.6)$$

This gives a good estimate of the object's Fourier modulus. If the reference star is bright enough and with the same seeing conditions.

High-resolution information, including spatial frequencies beyond the seeing cut-off, can be extracted from the object's Fourier modulus estimate. For a binary star system, this manifests as equally spaced fringes whose inclination angle reflects the orientation of the binary.

After obtaining the object's Fourier modulus, to extract information about the binary like separation, orientation, and intensity ratio, a fitting is made using this equation

$$O(\mathbf{u}) = A^2 + B^2 + 2AB\cos(2\pi\boldsymbol{\rho} \cdot \mathbf{u}) \quad (2.7)$$

where A is the intensity of the primary star, B is the intensity of the secondary star, ρ is the separation between the stars, and \mathbf{u} is two dimensional spatial frequencies. In order to recover the parameters of the model from the data, `scipy.optimize.curve_fit` [32] is used.

`scipy.optimize.curve_fit` utilises a non-linear least-squares fitting of data to a model. This function estimates the parameters of a model by minimizing the squared difference between the observed data and the model using the Levenberg–Marquardt algorithm [33]. It returns both the optimal parameter values and the estimated covariance matrix, enabling further analysis of parameter uncertainties. This tool is particularly useful for fitting simulation outputs to empirical or theoretical models and was applied in this study to extract key parameters from computational datasets.

The algorithm is sensitive to initial estimates of the parameters and can converge to a local minimum. To ensure good initial estimates are chosen, the ACF is used for the initial estimate of parameters. As mentioned in section 1.1.2, the ACF has a central peak and two lateral peaks, the separation from the central peak to a lateral peak is used as the initial ρ for the algorithm. To accurately extract the intensities of the primary and secondary stars from the lateral lobes, the ACF is first be rotated such that the lateral peaks are aligned horizontally. A one-dimensional slice is then taken through the centre of the rotated ACF to estimate the peak intensities. The orientation of the binary system is determined by rotating the object's Fourier modulus through 180° in 1° increments. At each step, the vertical columns of the rotated modulus are averaged to generate a one-dimensional projection. The contrast of this projection is calculated at each iteration, and the angle corresponding to the maximum contrast is taken as the binary star's orientation. The ACF is then rotated by this angle to align the peaks for analysis. The ACF is then averaged vertically to find the x-component of ρ , similarly the ACF is averaged horizontally to find the y-component of ρ . Unknown intensities A and B are chosen by solving the following simultaneous equations

$$A^2 + B^2 = I_{primary} \quad (2.8)$$

$$2AB = I_{secondary} \quad (2.9)$$

where $I_{primary}$ is the intensity of the central peak and $I_{secondary}$ is the intensity of one of the lateral peaks.

2.3 Photon Limited Conditions

In astronomy, the most interesting objects are usually very faint. Naturally SI has a fundamental limitation when the number of photons detected (photoevents) are limited. This work investigates whether the performance of SI as photoevents decrease and can GLAO improve this performance. Therefore, it's important to simulate low-light level conditions in a controllable manner. Negrete-Regagnon [35] describes a method of generating photon-limited speckle images. Speckle frames are generated in the usual manner. Then, the

normalized cumulative sum of the frame is taken and interpreted as the cumulative distribution function (CDF) representing the likelihood of photoevents occurring. To simulate each photoevent, a uniformly distributed random number in the range $[0, 1]$ is generated and used to sample the cumulative intensity distribution. This determines the pixel location for photon assignment. One count is then added to that pixel. This process is repeated until the total desired number of photons, K , has been distributed. The resulting low-light-level image is constructed by reshaping the array of photon counts back into the original image dimensions.

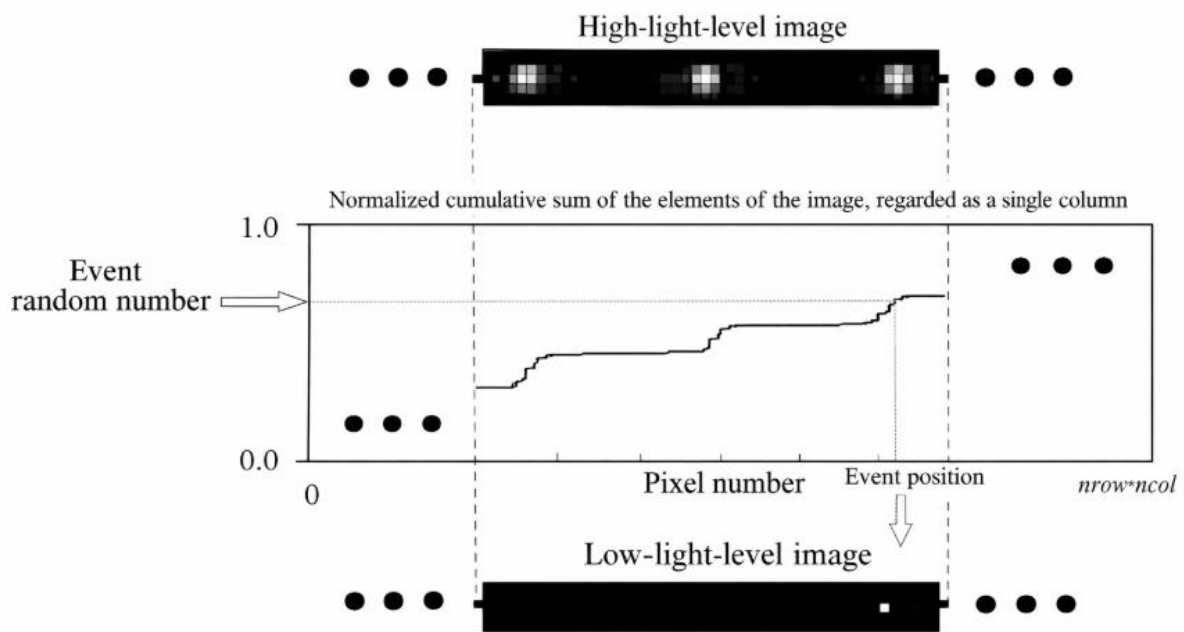


Figure 2.2: Illustration of low light level image generation [29].

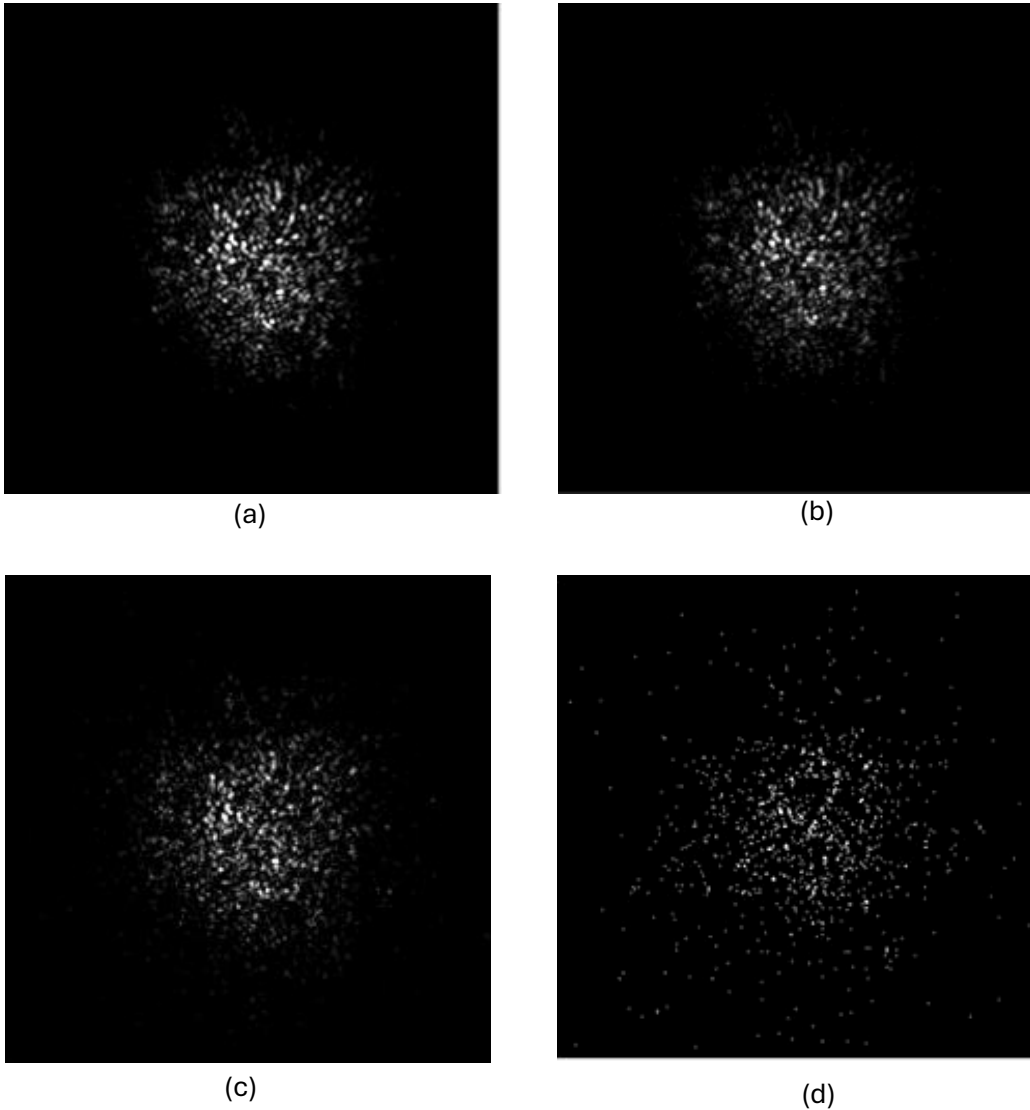


Figure 2.3: Generation of photon limited speckle images.
 (a) 1000000 photoevents, (b) 100000 photoevents, (c)
 10000 photoevents, (d) 1000 photoevents.

All simulated speckle images correspond to a field of view of approximately 6.6"x6.6" at a wavelength of 500 nm, based on a 4 m pupil sampled with 128 pixels across the diameter

2.4 Power Spectrum Signal-to-Noise Ratio

The Singal-to-Noise (SNR) ratio of the PS is a statistical approach to determine the quality of the PS. SNR becomes particularly important in photon limited conditions. In this section, the SNR of the PS is detailed.

In order to obtain an expression for SNR, the measured image can be modelled as

$$d_n(x, y) = \sum_{k=1}^{K_n} \delta(x - x_k, -y_k) \quad (2.10)$$

where $d_n(x, y)$ is the detected signal, $\delta(x - x_k, y - y_k)$ is the k^{th} photoevent occurring on the detector, and K_n is the total number of photoevents. Taking the FT of this leads to

$$\begin{aligned} D_n(u, v) &= \iint_{-\infty}^{\infty} d_n(x, y) \exp[-i2\pi(ux + vy)] dx dy \\ &= \sum_{k=1}^{K_n} \exp[-i2\pi(ux + vy)] \end{aligned} \quad (2.11)$$

Dainty and Greenway [36] defined an unbiased estimator for the PS of a set of photon-limited images as

$$Q_n(u, v) = |D_n(u, v)|^2 - K \quad (2.12)$$

where K is the number of photoevents in the image.

Typically, the SNR is expressed by

$$SNR = \frac{\text{mean value of quantity}}{\text{standard deviation of quantity}} \quad (2.13)$$

Considering frequencies higher than half the diffraction limited cutoff frequency, the single frame SNR for the unbiased estimator is

$$\begin{aligned} SNR_1 &= \frac{\langle Q_n(u, v) \rangle_N}{\sigma_{Q_n(u, v)}} \\ &= \frac{\langle Q_n(u, v) \rangle_N}{\{\text{var}[Q_n(u, v)]\}^{1/2}} \\ &= \frac{\langle Q_n(u, v) \rangle_N}{\{[\langle Q_n(u, v)^2 \rangle_N - \langle Q_n(u, v) \rangle_N^2]\}^{1/2}} \end{aligned} \quad (2.14)$$

Single frames can be divided into two categories according to [35]:

1. for high-light levels,

$$SNR_1(u, v) \approx 1; \quad (2.15)$$

2. for low-light levels

$$SNR_1(u, v) = \frac{\bar{K}}{n_s} \hat{H}_0(u, v) |\hat{O}(u, v)|^2, \quad (2.16)$$

where circumflexes denotes normalization, \bar{K} is the average number of photons per image, n_s is the average number of speckles per image defined as $n_s = \left(\frac{D}{r_0}\right)^2 / 0.435$, according to [30], $\hat{H}_0(u, v)$ is the normalised, diffraction limited, aberration free OTF of the telescope.

2.5 Bispectrum Signal-to-Noise Ratio

As in the case of the power spectrum SNR, low photon levels detected in an image can cause undesired, frequency-dependent photon bias in the bispectrum [35]. Using the image model of Equation (2.10), the average bispectrum of photon limited speckle images is given by

$$\begin{aligned} \langle D_n^{(3)}(u_1, v_1, u_2, v_2) \rangle = & \bar{K} + \bar{K}^2 \left[\langle |\hat{I}_n(u_1, v_1)|^2 \rangle + \langle |\hat{I}_n(u_1, v_2)|^2 \rangle + \langle \hat{I}_n^*(u_1, v_1, u_2, v_2) \rangle \right] \\ & + \bar{K}^3 \langle \hat{I}_n^{(3)}(u_1, v_1, u_2, v_2) \rangle \end{aligned} \quad (2.17)$$

where $\langle |\hat{I}_n(u_1, v_2)|^2 \rangle$ and $\langle \hat{I}_n^{(3)}(u_1, v_1, u_2, v_2) \rangle$ are the normalized power spectrum and bispectrum of the speckle image respectively. Wirnitzer [37] showed that one way to evaluate an unbiased bispectrum estimate is to evaluate

$$\begin{aligned} Q_n^{(3)}(u_1, v_1, u_2, v_2) = & D_n^{(3)}(u_1, v_1, u_2, v_2) - \\ & [|D_n(u_1, v_1)|^2 + |D_n(u_2, v_2)|^2 + D_n^*(u_1 + u_2, v_1 + v_2) - 2K_n] \end{aligned} \quad (2.18)$$

The expected value is given by

$$\langle Q_n^{(3)}(u_1, v_1, u_2, v_2) \rangle = \bar{K}^3 \langle \hat{I}_n^{(3)}(u_1, v_1, u_2, v_2) \rangle \quad (2.19)$$

Following a similar analysis to the power spectrum SNR, the bispectrum SNR is given by

$$SNR_1^{(3)}(u_1, v_1, u_2, v_2) = \frac{\langle Q_n^{(3)}(u_1, v_1, u_2, v_2) \rangle}{\sigma_{Q_n^{(3)}}} \quad (2.20)$$

Like the power spectrum SNR, there are two cases to consider:

1. for high-light levels,

$$SNR_1^{(3)}(u_1, v_1, u_2, v_2) \approx 1; \quad (2.21)$$

2. for low-light levels

$$SNR_1^{(3)}(u_1, v_1, u_2, v_2) = \frac{\bar{K}^{\frac{3}{2}}}{n_s} \hat{T}_0^{(3)}(u_1, v_1, u_2, v_2) \hat{O}(u_1, v_1, u_2, v_2), \quad (2.22)$$

where $\hat{T}_0^{(3)}(u_1, v_1, u_2, v_2)$ is the normalised, diffraction-limited, aberration-free bispectral transfer function.

Equation (2.20), which incorporates the total bispectral variance $\sigma_{I^{(3)}}^2 = \sigma_R^2 + \sigma_I^2$ representing the variances of the real and imaginary components, respectively—may not be the most informative. This is because such a formulation does not adequately capture how each component independently contributes to fluctuations in the signal. A more precise assessment of phase-related SNR can be obtained by analysing the variability perpendicular to the average direction of the complex signal in the complex plane. This approach considers the dispersion orthogonal to the signal's mean vector, offering a phase-specific measure of noise.

Since the object's Fourier modulus is got through SI techniques, the bispectrum is usually applied to phase recovery, so for the accurate single frame bispectral phase SNR is given by

$$SNR_1^\beta = \frac{|\langle I_n^{(3)} \rangle|}{[\sigma_I^2 \cos^2(\beta) + \sigma_R^2 \sin^2(\beta) - Cov(I, R) \sin(2\beta)]^{\frac{1}{2}}} \quad (2.23)$$

This equation is used as weighting described below. A more detailed derivation of the single frame bispectral phase SNR is given in [35]

2.6 Fourier Phase Recovery

To recover the object phase, the bispectrum of each short-exposure image is calculated by Equation (1.11). The bispectrum is a function of two frequencies (u_1 and u_2) that describes the

correlation between these frequencies and their sum ($u_1 + u_2$). It works by combining three points in the image's Fourier transform in a special way that cancels out the random changes caused by turbulence. The object phase spectrum is encoded in the bispectral phase by the relationship in Equation (1.13). A least-squares minimization procedure, outlined in Glindemann et.al [38], was employed in this work.

They described a model for the special case of a binary star that's described by

$$b(\mathbf{x}) = \delta(\mathbf{x}) + A\delta(\mathbf{x} - \mathbf{p}) \quad (2.24)$$

where the intensity of the primary star = 1 at $\mathbf{x} = 0$, and the intensity of the secondary star = A, and is located at $\mathbf{x} = \mathbf{p}$. Its power spectrum can therefore be described by

$$B(\mathbf{u}) = 1 + A \exp(i2\pi\mathbf{u} \cdot \mathbf{p}) \quad (2.25)$$

and its bispectrum is given by Equation (1.11), which for this case can be written as

$$B(\mathbf{u}_1, \mathbf{u}_2) = B(\mathbf{u}_1)B(\mathbf{u}_2)B(-\mathbf{u}_1 - \mathbf{u}_2) \quad (2.26)$$

To find A and \mathbf{p} , the following equation needs to be minimized

$$\sum_1^M [\text{mod } 2\pi(\psi_{i,j} - \beta_{i,j})]^2 \text{SNR}_{i,j} \quad (2.27)$$

where the SNR is calculated using Equation (2.23), $\psi_{i,j}$ is the measured bispectral phase, and $\beta_{i,j}$ is the phase from the model bispectrum in Equation (2.26).

Glindemann noted that using a least-squares minimization procedure on Equation (2.27) contains multiple minima. Using measurements from a power spectrum drastically improved its convergence to the true minima.

In this work, Equation (2.7) is used to recover the binary parameters and Equation (2.27) is used to determine the correct orientation of the binary (as mentioned in section 1.1.2, there is an 180° ambiguity in the orientation of the binary star in the PS).

2.7 Ground Layer Adaptive Optics System

The AO system chosen for this work employed the work of Noll [39]. The phase screen imparts phase deviations to the wavefront. This perturbed wavefront can be decomposed and

reconstructed using Zernike polynomials. A wave function, φ , defined over a unit circle can be approximated as a finite sum of Zernike polynomials as

$$\varphi(R\rho, \theta) = \sum_{j=0}^J a_j Z_j(\rho, \theta) \quad (2.28)$$

where R is the radius of the circle, $0 \leq \rho \leq R$, J is the maximum number of Zernike terms, $Z_j(\rho, \theta)$ is the j^{th} -term of the Zernike polynomials, and a_j is the expansion coefficient which is given by

$$a_j = \int d^2\rho W(\rho) \varphi(R\rho, \theta) Z_j(\rho, \theta) \quad (2.29)$$

where $W(\rho)$ is the aperture weighting function.

AOtools has a class designed to create an array of Zernike polynomials using Noll indices. Figure 2.4 below shows the first few terms of the Zernike polynomials

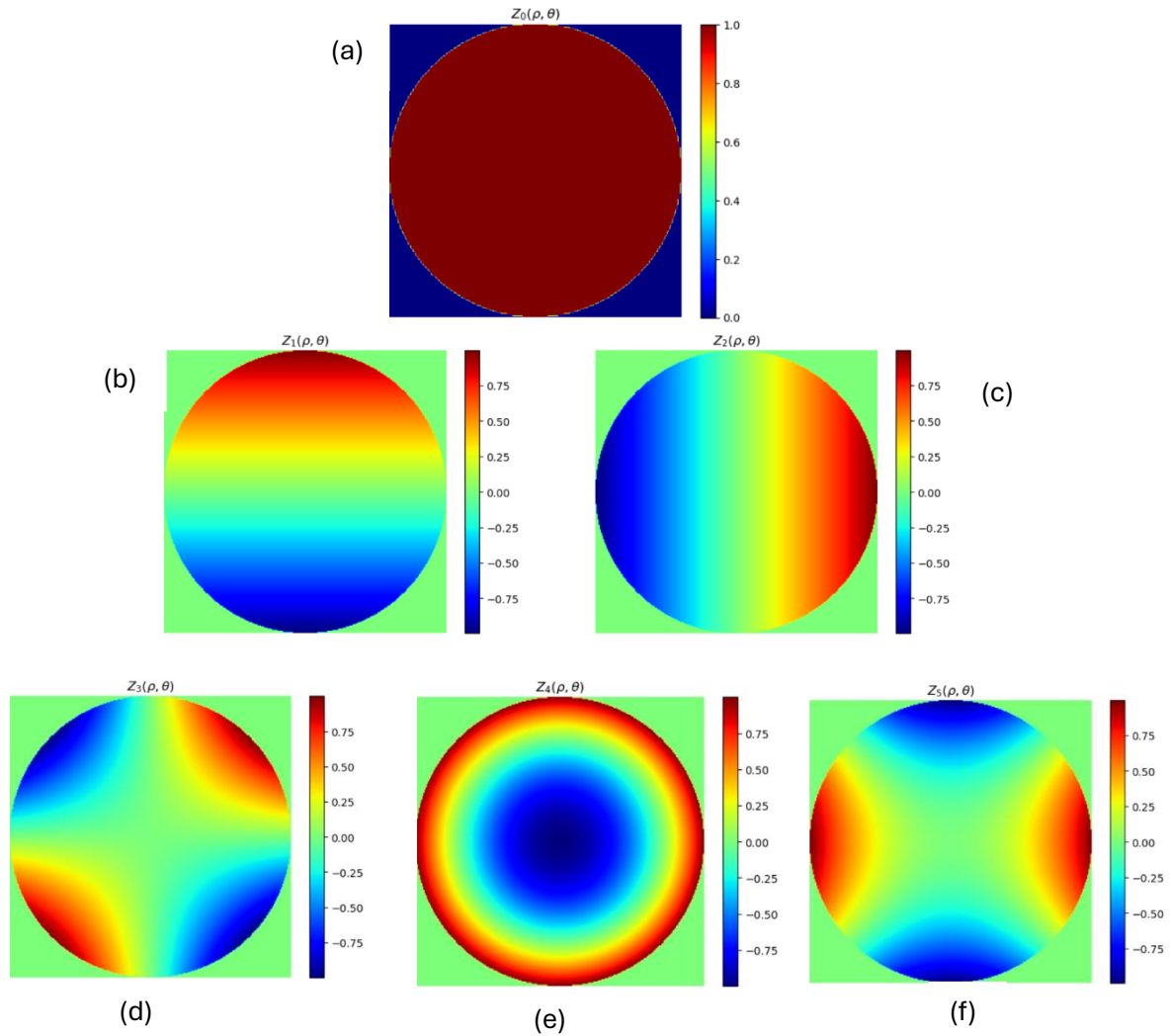


Figure 2.4: The first six Zernike polynomials generated using AOtools. (a) Piston, (b) Horizontal Tilt, (c) Vertical Tilt, (d) Oblique Astigmatism, (e) Defocus, (f) Astigmatism.

To reconstruct the perturbed wavefront using Zernike polynomials, the wavefront is projected onto a Zernike basis; the phase screen is multiplied by each Zernike term and summed. Each term is then normalised. This results in finding the expansion coefficients of each term of the phase screen. Once the expansion coefficients are found, the phase screen can be rebuilt using Equation (2.28).

Simulating AO is simply a matter of setting several Zernike modes to zero. Roddier [30] noted that to reconstruct the wavefront perfectly, an infinite amount of Zernike polynomials would need to be included. This approach is an approximate as AO systems do not work like this in reality – their ability to correct wavefronts is determined by factors including signal to noise in the wavefront sensor, the number of actuators in the deformable and the temporal response of the system.

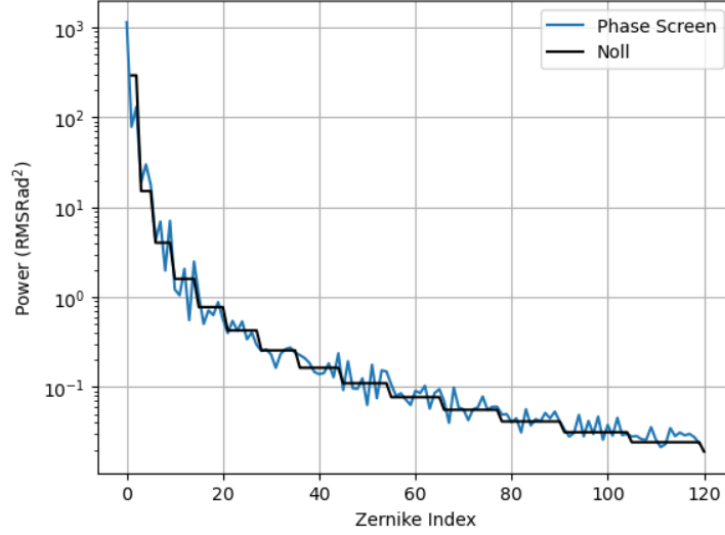


Figure 2.5: Zernike breakdown over 1000 Kolmogorov phase screens generating using AOtools.

Figure 2.5 shows the variance of the expansion coefficients after the phase screen was projected onto 120 Zernike modes. The black line shows the theoretical Kolmogorov values from Noll [39]; they are in good agreement with each other and proves that the phase screen used follows the expected power laws.

2.8 Simulation Set-Up

Simulation of short exposure images of a binary star system degraded by the atmosphere was set up as follows:

A 128x128 Kolmogorov phase screen generated by AOtools with the configuration given in table 2.1.

Table 2.1: Input parameters for the phase screen generated by AOtools.

Number of pixels	128
Size (m)	4
Pixel Scale (m)	4/128
Outer Scale (m)	100
λ (nm)	500
r_0 – Ground Layer (m)	0.20
r_0 – Upper Layer (m)	0.40

A 2D wavefront, $\varphi(x, y)$, that was perturbed by the atmosphere was simulated at the telescope pupil using

$$\varphi(x, y) = e^{i(\phi_{GL}(x, y) + \phi_{UL}(x, y))} \quad (2.30)$$

where $\phi_{GL}(x, y)$ is the ground layer phase screen, which was used for correction, and $\phi_{UL}(x, y)$ is the upper layer phase screen. Adding two phase screens into one phase screen gave an effective $r_0 = 0.17$ m. This was calculated using the following formula [41]

$$r_{0,eff} = \left[r_{0,GL}^{\frac{-5}{3}} + r_{0,UL}^{\frac{-5}{3}} \right]^{-\frac{3}{5}} \quad (2.31)$$

A 128x128 pupil mask was generated using AOtools shown in figure 2.6. A 4 m main mirror and a 0.5 m secondary mirror was created. The pupil mask and phase screen were padded by a factor of two to ensure that the Fourier analysis of the speckle images satisfied Nyquist sampling, i.e., the sampling frequency was at least twice the highest spatial frequency present. The wavefront was then multiplied by this pupil mask to produce the aperture function, and a 2-D Fourier transform of the aperture function yielded the image formed at the telescope's focal plane. The pixel size in the focal plane was calculated using the following equation:

$$a = \frac{\lambda}{2D} \quad (2.32)$$

where D is the diameter of the telescope, λ is the wavelength of light. The factor 2 is there because the aperture is twice padded. For this work $\lambda = 500$ nm and $D = 4$ m, resulting in a pixel size of

$$a = 206265 \frac{500 \times 10^{-9}}{2(4)} = 0.01289 \text{ "}$$

where the multiplicative factor is for conversion from radians to arcseconds.

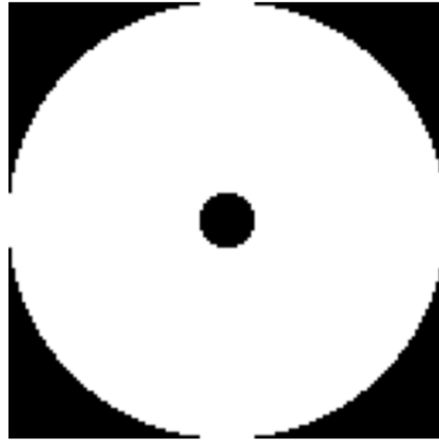


Figure 2.6: Simulated 4m primary mirror and a 0.5m secondary mirror telescope generated using AOtools.

A set of one thousand binary star images was simulated by duplicating the point source (primary star) created from the Fourier transform of the aperture function. This duplicate was shifted by (x, y) pixels to represent a binary with a position angle $\arctan(y/x)$ and a separation of $(x^2+y^2)^{1/2}$, scaled by a factor less than or equal to one to model the fainter secondary star, and then added to the original image.

Chapter 3 Results

This chapter presents the results of the simulations and analyses described in Chapter 2.

3.1 Speckle Image Generation

Several simulated speckle images of a binary star system are presented in Figure 3.1, each illustrating varying degrees of atmospheric turbulence. Figure 3.1(a) shows a diffraction-limited image of a binary system with an equal intensity ratio of 1:1. Figures 3.1(b), 3.1(c), and 3.1(d) demonstrate the effect of atmospheric turbulence, where each speckle image consists of many randomly shifted diffraction-limited copies of the object. As clearly observed, the number of speckles increases as the Fried parameter r_0 decreases, which is consistent with the theoretical relationship described in Figure 1.1.

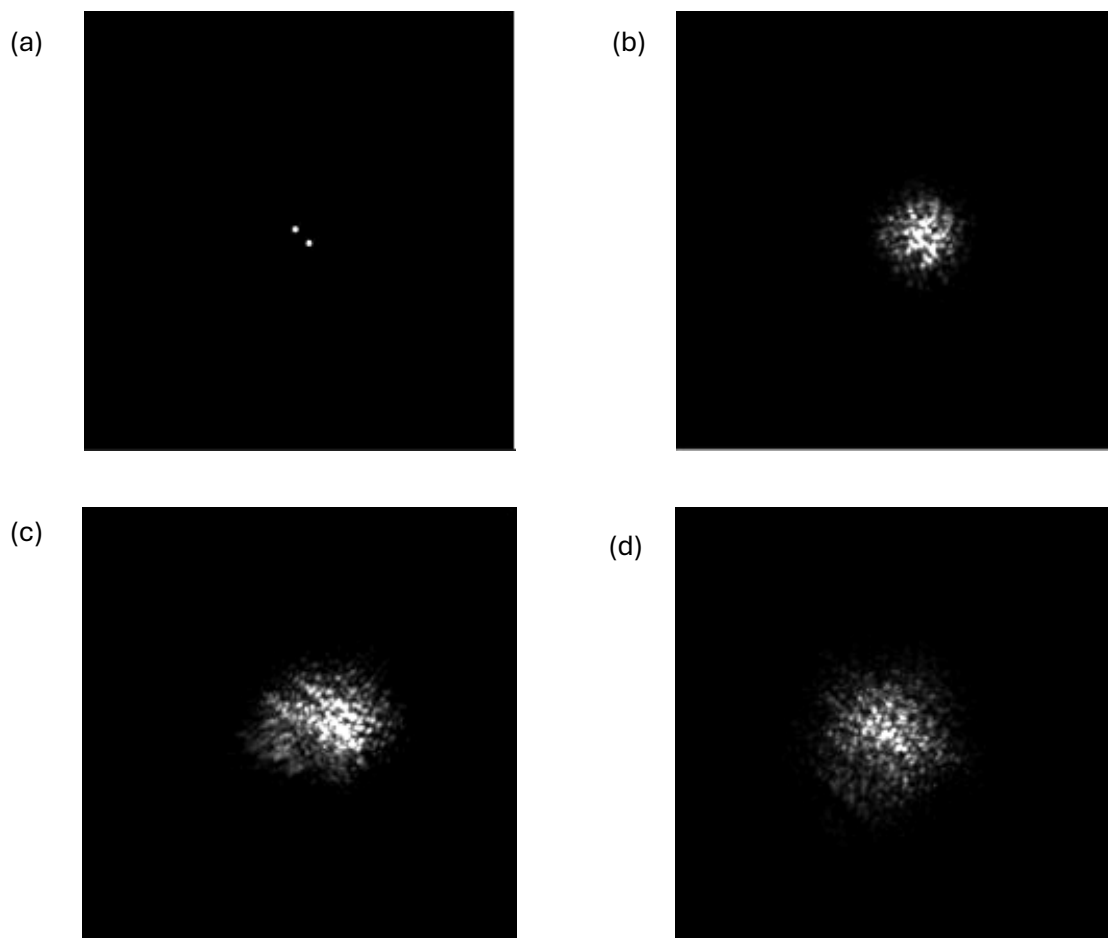
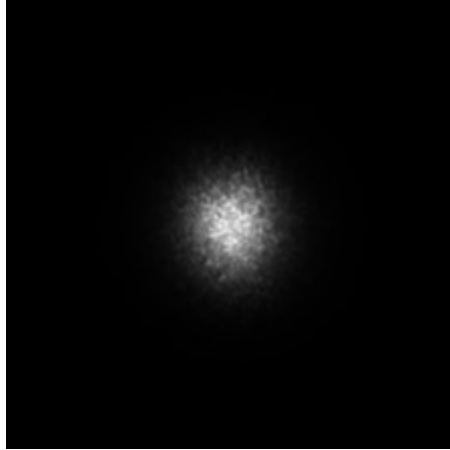


Figure 3.1: Speckle images of a binary star system with two million photoevents. (a) diffraction limited, (b) $r_0 = 0.25$ m, (c) $r_0 = 0.20$ m, (d) $r_0 = 0.15$ m. Separation = $0.077''$, orientation = 135° .



*Figure 3.2: Long exposure image of a binary star system.
Same configuration as Figure 3.1 (c).*

In contrast, Figure 3.2 shows a long-exposure image of the same binary system in Figure 3.1(c), where the 2000 speckle images have been averaged into a smooth "seeing disk" with an angular width proportional to λ/r_0 , as detailed in section 1.1.1. As atmospheric turbulence increases (i.e., as r_0 decreases), the diameter of the seeing disk grows. It is important to note, even under poor seeing conditions, speckle images retain high spatial frequency content. This highlights that speckle imaging remains diffraction-limited rather than seeing-limited, in contrast to long-exposure imaging.

3.2 Power Spectrum Calibration

This section describes results from recovering an estimate for the calibrated object PS.

Figure 3.3 displays a PS acquired with simulated seeing conditions of $r_0 = 0.20$ m in addition to a diffraction-limited PS for comparison for both a reference star and a binary star. The configuration for the binary was as follows: intensity ratio = 1, separation = 0.047 arcseconds, and orientation = 0° . Two million photoevents were generated for both reference and binary stars. The zeroth frequency was shifted to the centre for all spectra shown.

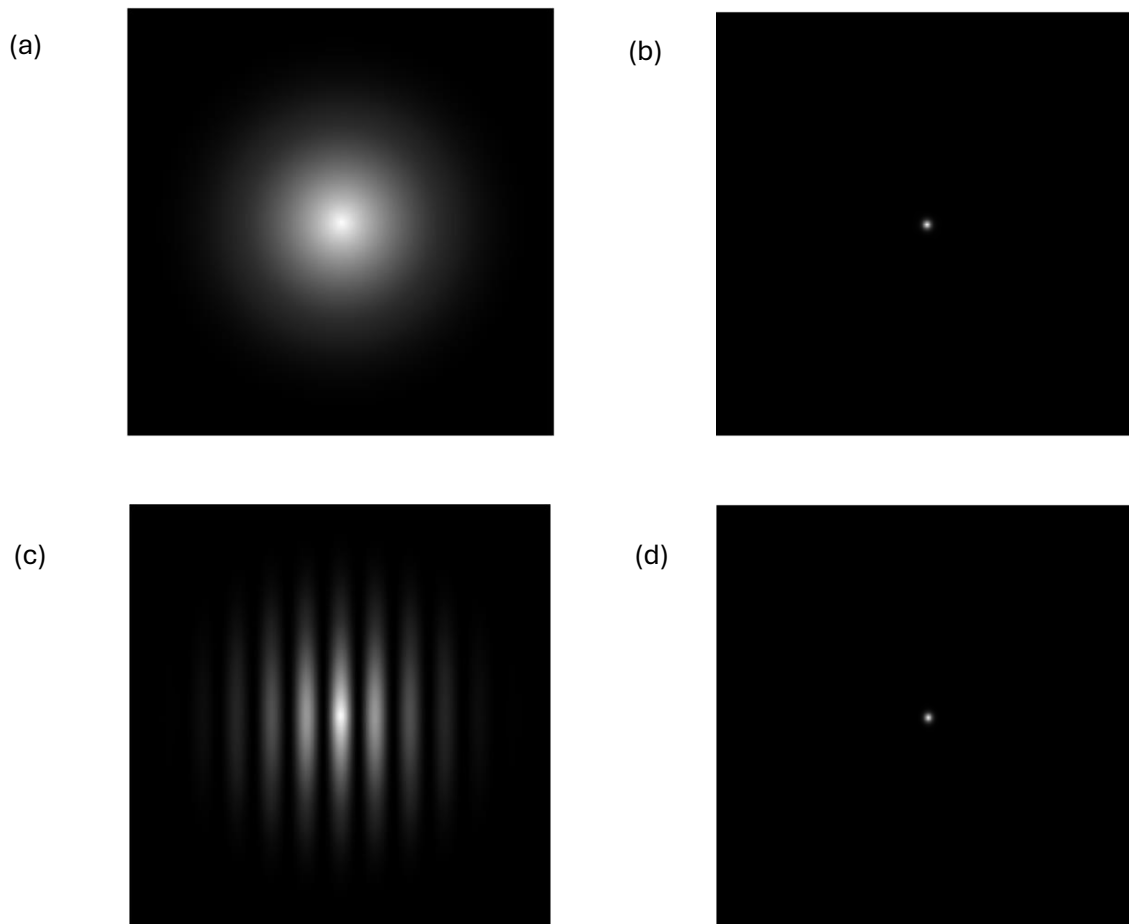


Figure 3.3: (a) and (c) are diffraction limited PS of a reference star and binary star respectively. (b) and (d) are PS of the reference star and binary star corresponding to a $r_0 = 0.17$ m and $K = 2,000,000$, separation = $0.077''$, orientation = -270° .

In relation to reference star, the power spectrum exhibited the expected characteristics of a point source, clearly illustrating how higher spatial frequencies are progressively attenuated as the Fried parameter r_0 decreases. In the case of ideal (diffraction-limited) conditions, the power spectrum was bounded only by the diffraction cut-off frequency, u_c . However, under degraded seeing conditions with $r_0 = 0.17$ m, the effective cut-off frequency, u_s , was reduced significantly. This reduction reflects the narrowing of the ensemble-averaged transfer function term $H(u,v)$, which approaches zero for spatial frequencies $u > u_s$. Since u_s scales inversely with r_0 , poor seeing conditions severely limit the system's ability to preserve high spatial frequency content [4]. As a result, all spatial frequencies beyond u_s are lost in the long-exposure image, corresponding to a significant degradation in image resolution and the loss of fine detail.

Dividing the reference PS by the object PS results in a calibrated PS shown in Figure 3.4 below. It produced the characteristic sinusoidal fringes. The calibrated PS exhibited spatial frequencies extending up to the diffraction-limited cut-off, with no apparent attenuation due

to atmospheric seeing. This demonstrates that frequencies beyond the seeing-limited cut-off are still preserved in short-exposure speckle images.

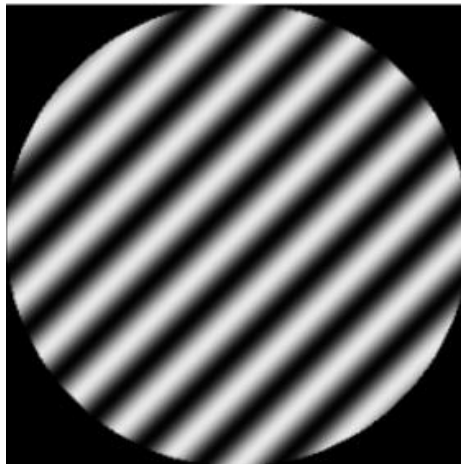


Figure 3.4: Calibrated object PS ($r_0 = 0.17$ m, $K = 2,000,000$, separation = $0.077''$, orientation = 45° , Intensity ratio = 1).

The following set of power spectrum images were generated using the same configuration as Figure 3.4, but with a reduced intensity ratio. These results demonstrate that as the intensity ratio increases (i.e., the secondary star becomes fainter), the fringe contrast diminishes, making them increasingly difficult to distinguish. It was determined that the limiting intensity ratio for fringe visibility when two million photoevents were detected was approximately 0.05.

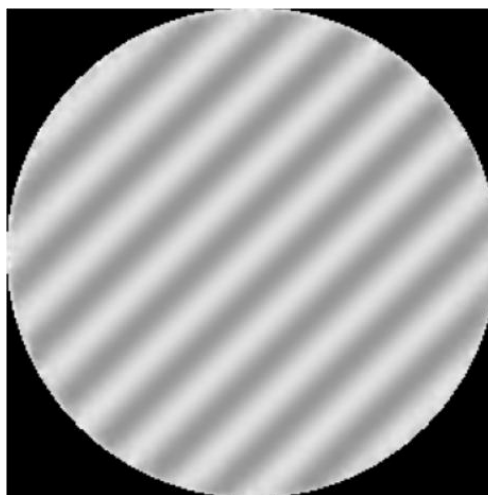
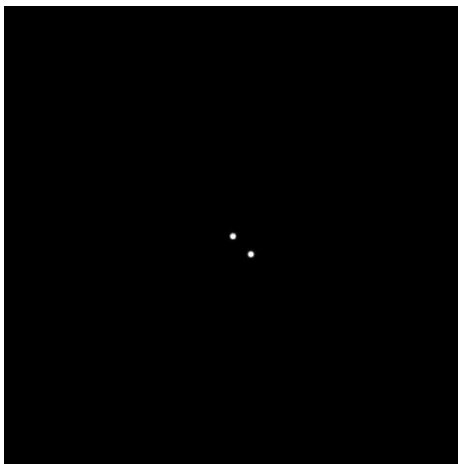


Figure 3.5: Intensity ratio = 0.1. Same configuration as Figure 3.4.

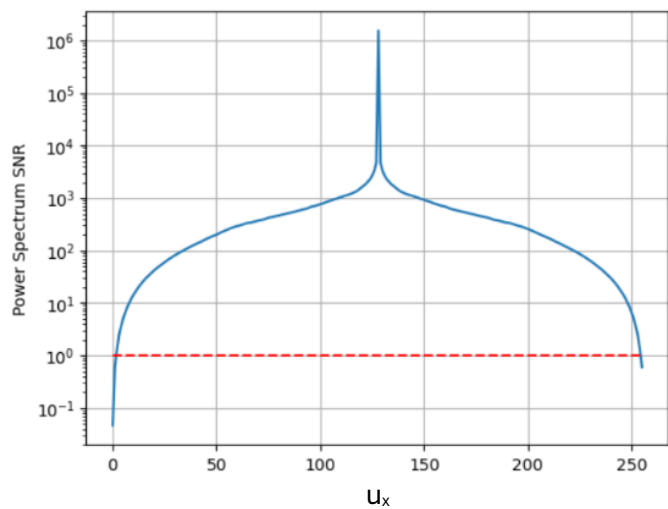
As clearly shown in Figure 3.5, reducing the intensity ratio significantly impacts the visibility of the fringes in the calibrated PS. In Figure 3.4, with an intensity ratio of 1.0, the fringes are discernible and display reasonably strong contrast. However, in Figure 3.5, where the intensity ratio is reduced to 0.1, the fringe contrast is markedly diminished. Despite the reduced visibility, the PS still exhibits spatial frequency components extending up to the diffraction limit cut-off frequency, indicating that high spatial frequency information is retained. This demonstrates that diffraction-limited information of the object remains encoded in the power spectrum.

Despite spatial frequencies extending to the diffraction limit cutoff frequency for large number of photoevents for binaries, this does not occur when the number of photoevents detected are limited. A quantitative way to look at it is through the power spectrum SNR. The following figures show the degradation of signal quality as the number of photoevents detected decreases

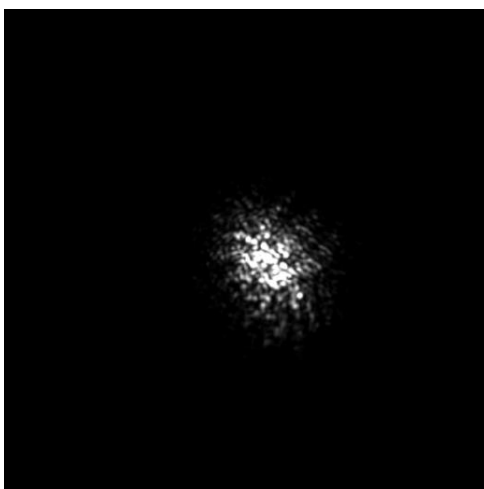
(a)



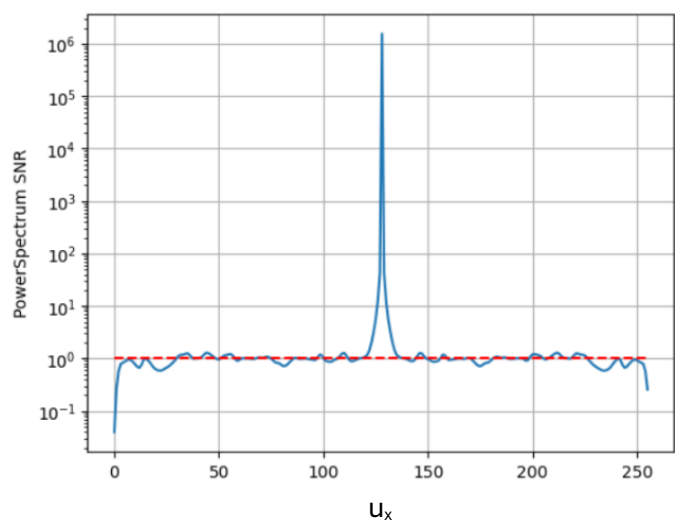
(b)



(c)



(d)



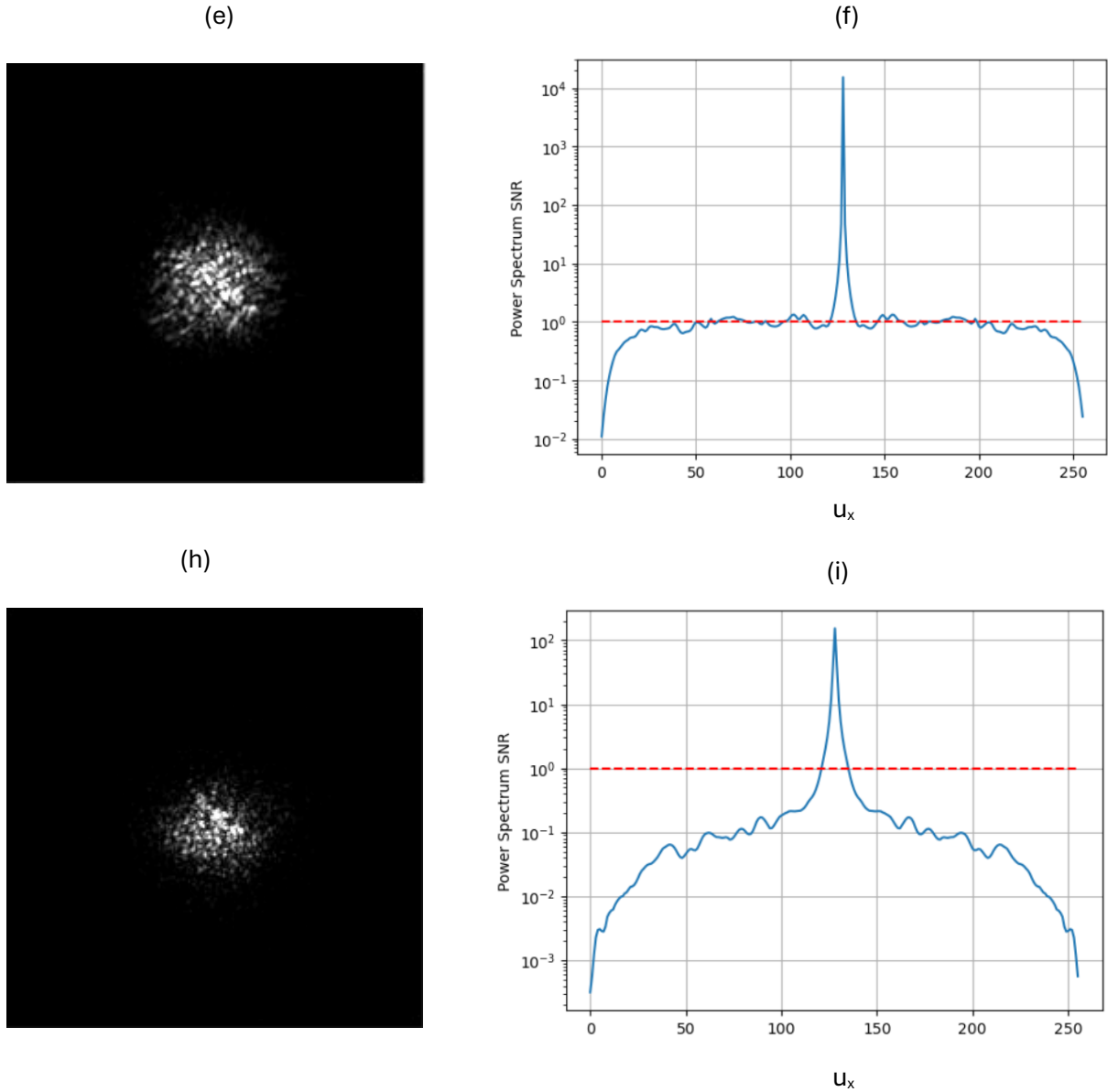


Figure 3.6: show the speckle image of binary stars and resulting power spectrum SNR of the reference star for 1,000,000, 100,000, and 10,000 photoevents. Separation = 0.077", orientation = 135°.

Figure 3.6 presents examples of simulated speckle images and their corresponding power spectrum SNR computed using Equation (2.14). Except for Figures 3.6(a) and 3.6(b), all speckle images share the same configuration: a Fried parameter $r_0 = 0.17\text{m}$, an intensity ratio of 1, a binary separation of 0.219 arcseconds, and an orientation of 45°. The SNR plots shown are one-dimensional slices taken through the centre of the power spectrum SNR and displayed on a logarithmic scale. The red dashed line indicates the high-light-level SNR limit, which is approximately equal to 1, as defined by Negrete-Regagnon [35]. Figure 3.6 demonstrates how the power spectrum SNR behaves under varying levels of photoevents.

Figures 3.6(a) and 3.6(b) correspond to the diffraction-limited case, where 1,000,000 photoevents were detected. As expected, the power spectrum SNR retains high contrast across all spatial frequencies up to the diffraction cut-off u_c . For speckle images atmospherically degraded, it is seen that when one million photoevents are detected, the power spectrum SNR remains relatively flat, indicating reliable signal throughout, as seen in Figure 3.6(d). As the number of photoevents decreases across the subsequent examples, a clear decline in the SNR is observed. This reduction in SNR has significant implications for binary parameter extraction: in the binary fitting model, the SNR from Figure 3.6 is used as a weighting function in the `scipy.optimize.curve_fit` algorithm. Only data points with SNR values above the red dashed line are retained for the fitting procedure; data below this threshold are excluded, ensuring that the model prioritizes high-confidence spatial frequencies.

3.3 Autocorrelation Function

The ACF played a critical role in the recovery of the binary parameters. Figure 3.7 below shows an example of an ACF and an 1D slice of the ACF after it was rotated 45° , where $K = 100,000$, $\rho = 0.219$ arcseconds, $\theta = 45^\circ$, and $I = 1.0$:

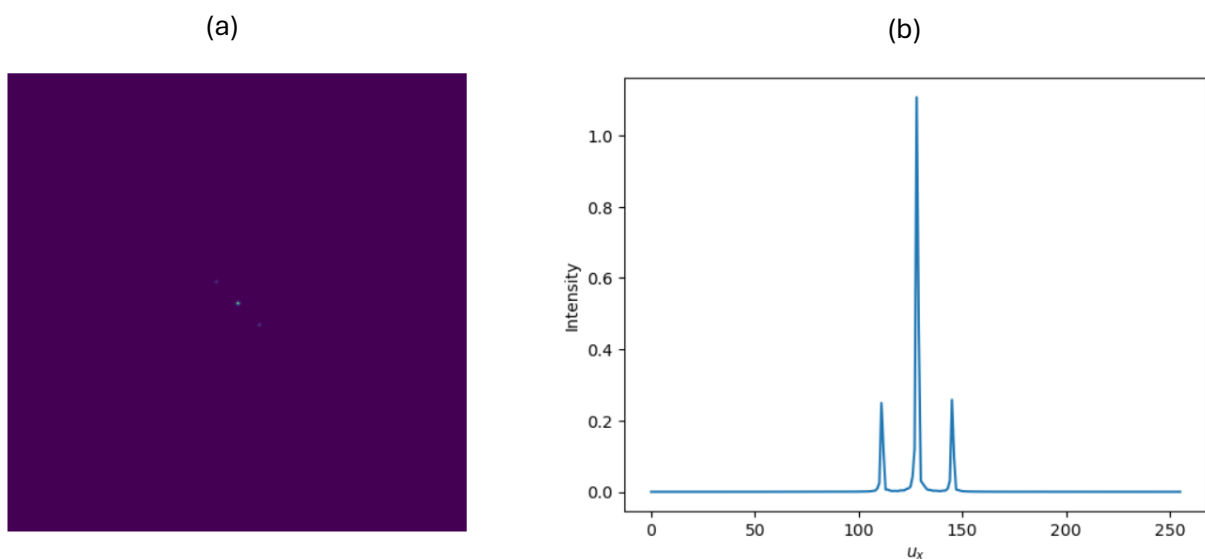


Figure 3.7: (a) ACF of a PS with the configuration where $K = 100,000$, $\rho = 0.219$ arcseconds, $\theta = 45^\circ$, and $I = 1.0$. (b) 1D cross section of ACF

From the ACF, the x - and y -components of the separation vector ρ were determined by identifying the locations of the lateral correlation peaks. In addition, preliminary estimates of the component intensities A and B can be obtained by solving Equations (2.8) and (2.9) using the relative peak amplitudes. In this example, the recovered estimates were 11.74 and 1.33, which deviate significantly from the expected values. Nevertheless, although the absolute estimates of A and B were inaccurate, the algorithm was able to recover the correct intensity ratio, demonstrating that estimates for the intensity ratio are not critical in the algorithm

3.4 Recovery of Binary Star Parameters

3.4.1 High Light Conditions

This section presents the results obtained from the binary star parameter extraction algorithm described in Chapter 2. The simulations were designed to assess the algorithm's accuracy in recovering the separation (ρ), position angle (θ), and relative intensity ratio (I) of the binary components from speckle interferometry data.

Each simulation was based on 1,500,000 detected photoevents per speckle image and used a simulated binary star system with known separation, orientation, and intensity parameters. The recovered parameters were compared directly to their simulated values to evaluate the performance of the method.

Simulation 1.1: $\rho = 0.077''$, $\theta = 270^\circ$

Figure 3.8 is the power spectrum SNR for the reference star receiving 1,500,000 photoevents. This graph shows that high spatial frequency information extends right up to the diffraction cut off frequency. In this case, all the spatial frequencies up to the diffraction cutoff frequency are used in the model. In the following sections, where there was a decrease in the number of photoevents, the power spectrum SNR begins to degrade.

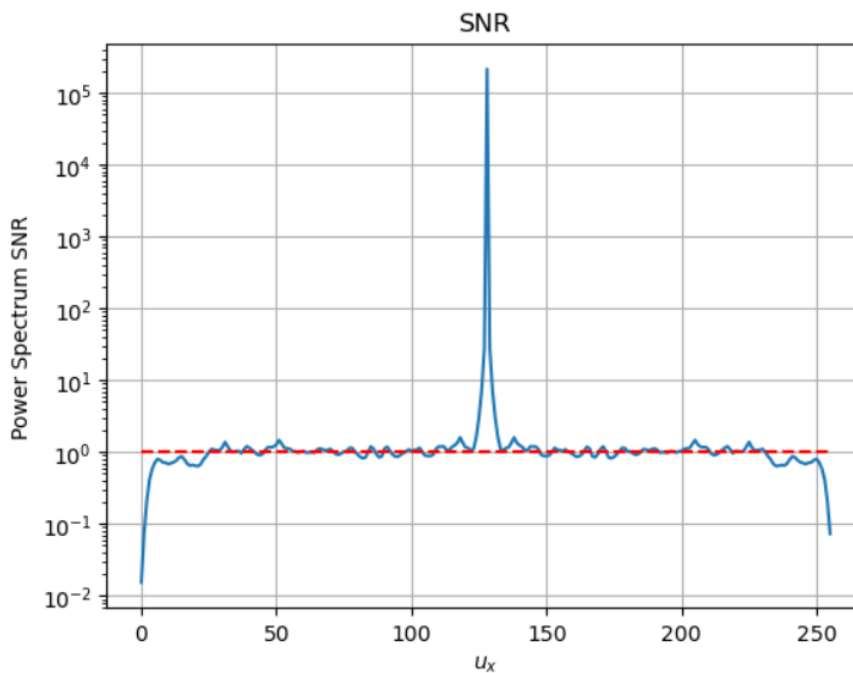


Figure 3.8: Power spectrum SNR of a reference star. $K = 1,500,000$. This graph is logarithmically scaled.

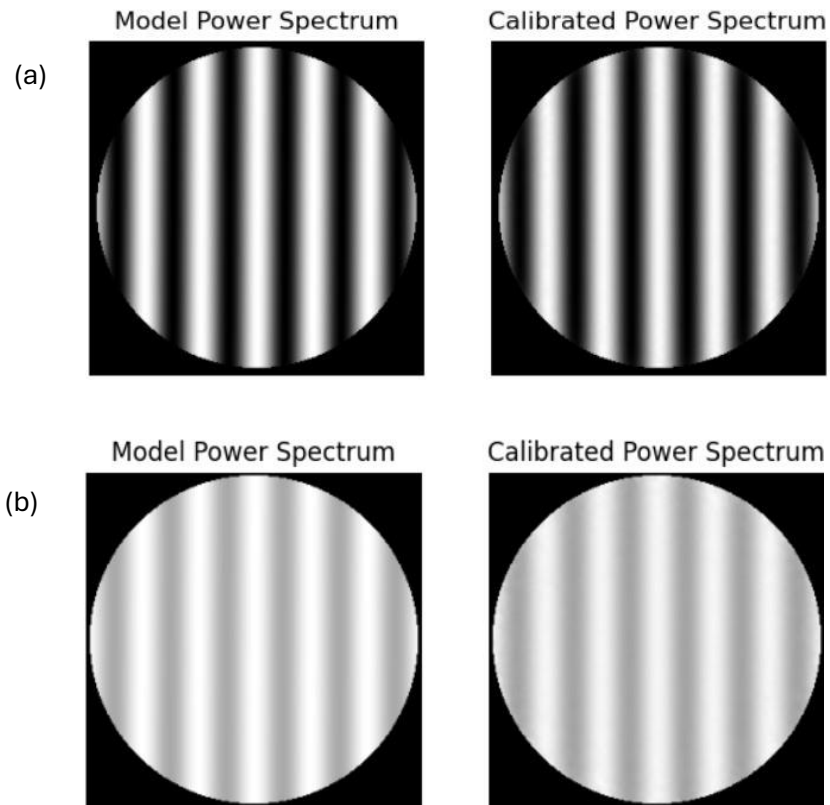


Figure 3.9: Model PS along with the calibrated PS. $\rho = 0.077''$, $\theta = 270^\circ$, $K = 1,500,000$. (a) $I = 1.0$, (b) $I = 0.1$.

The calibrated power spectrum and model power spectrum are shown here to illustrate the contrast change as the intensity ratio of the binary stars decreases.

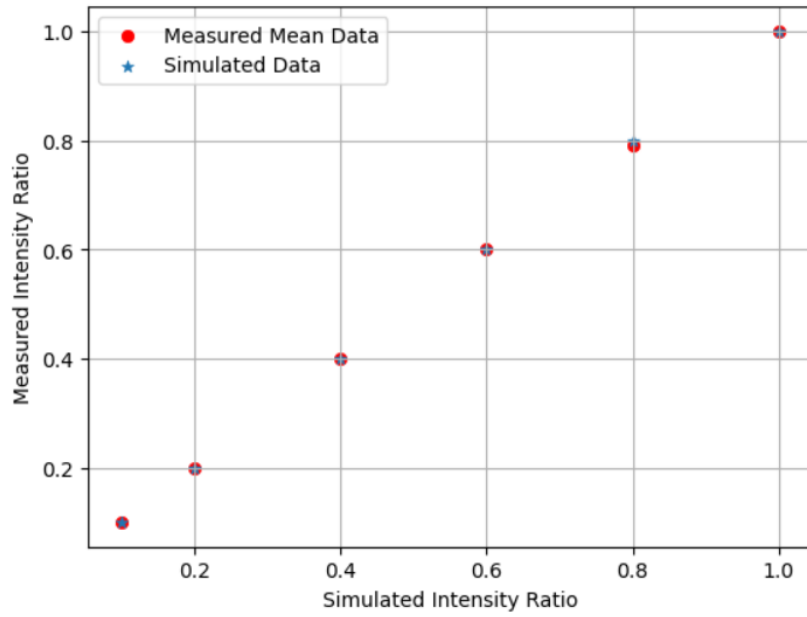
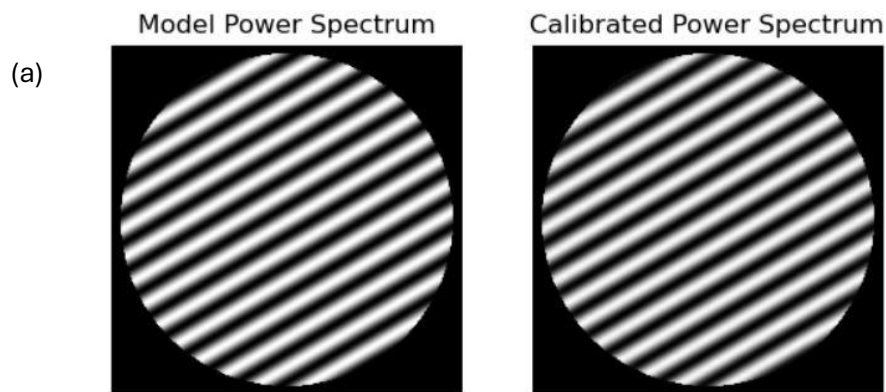


Figure 3.10: Recovered intensity ratios from the model under high photon condition. $\rho = 0.077''$, $\theta = 270^\circ$, $K = 1,500,000$.

Table 3.1: Recovered separation and orientation from the model for simulation 1.1. The average error is negligible, proving the algorithm's ability to recover binary star parameters under high-light conditions.

ρ (") (Simulated)	ρ (") (Measured)	θ (°) (Simulated)	θ (°) (Measured)	Average σ for Intensity
0.077	0.077	270.0	270.0	0.002741

Simulation 1.2: $\rho = 0.179''$, $\theta = 59.74^\circ$



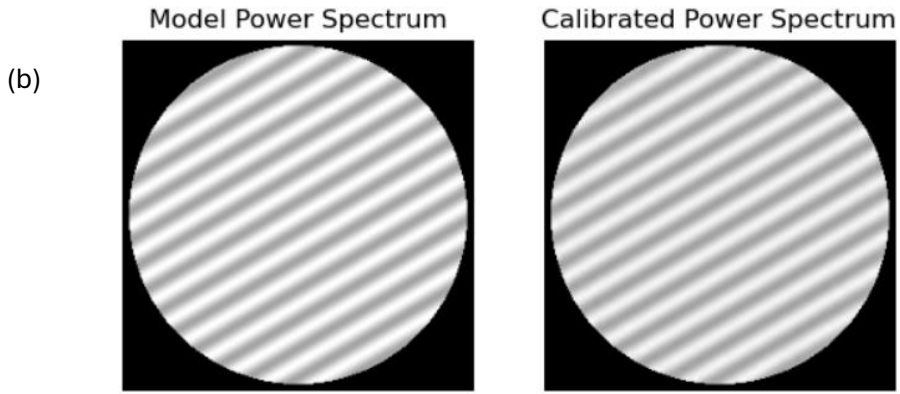


Figure 3.11: Model PS along with the calibrated PS. $\rho = 0.179''$, $\theta = 59.74^\circ$, $K = 1,500,000$. (a) $I = 1.0$, (b) $I = 0.1$.

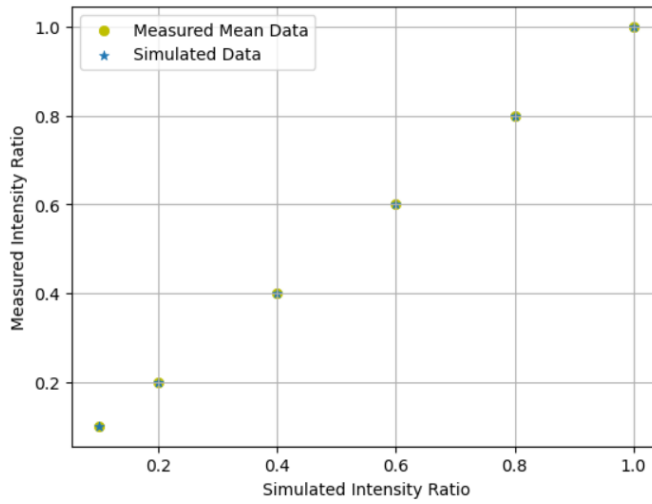


Figure 3.12: Recovered intensity ratios from the model under high photon condition. $\rho = 0.179''$, $\theta = 59.74^\circ$, $K = 1,500,000$

Table 3.2: Recovered separation and orientation from the model for simulation 2.1. The average error negligible, proving the algorithm's ability to recover binary star parameters under high-light conditions.

ρ (") (Simulated)	ρ (") (Measured)	θ (°) (Simulated)	θ (°) (Measured)	Average σ for Intensity
0.179	0.179	59.74	59.74	0.008003

Simulation 1.3: $\rho = 0.219''$, $\theta = 45.0^\circ$

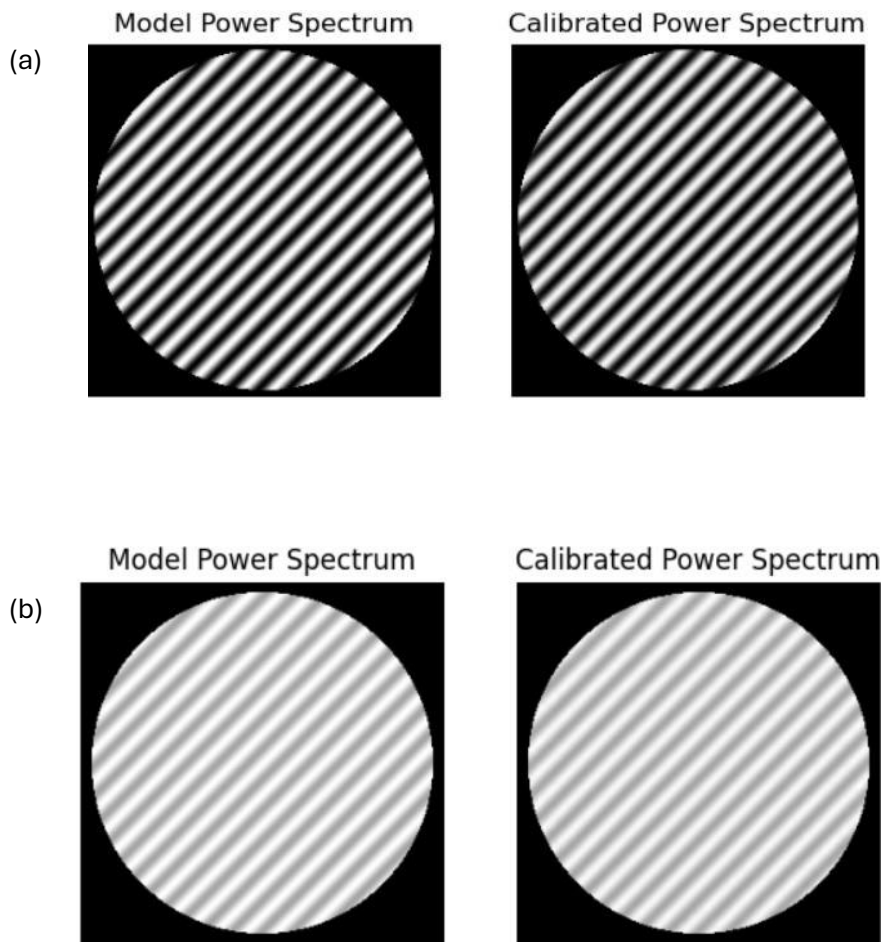


Figure 3.13: Model PS along with the calibrated PS. $\rho = 0.219''$, $\theta = 45^\circ$, $K = 1,500,000$. (a) $I = 1.0$, (b) $I = 0.1$.

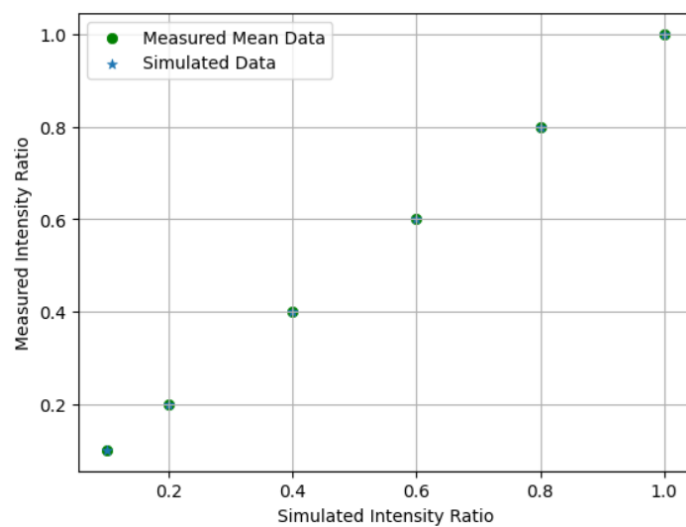


Figure 3.14: Recovered intensity ratios from the model under high photon condition. $\rho = 0.219''$, $\theta = 45^\circ$, $K = 1,500,000$.

Table 3.3: Recovered separation and orientation from the model for simulation 3.1 The average error is negligible, proving the algorithm's ability to recover binary star parameters under high-light conditions.

ρ (") (Simulated)	ρ (") (Measured)	θ (°) (Simulated)	θ (°) (Measured)	Average σ for Intensity
0.258	0.258	45.0	45.0	0.006639

Simulation 1.4: $\rho = 0.258''$, $\theta = 90.0^\circ$

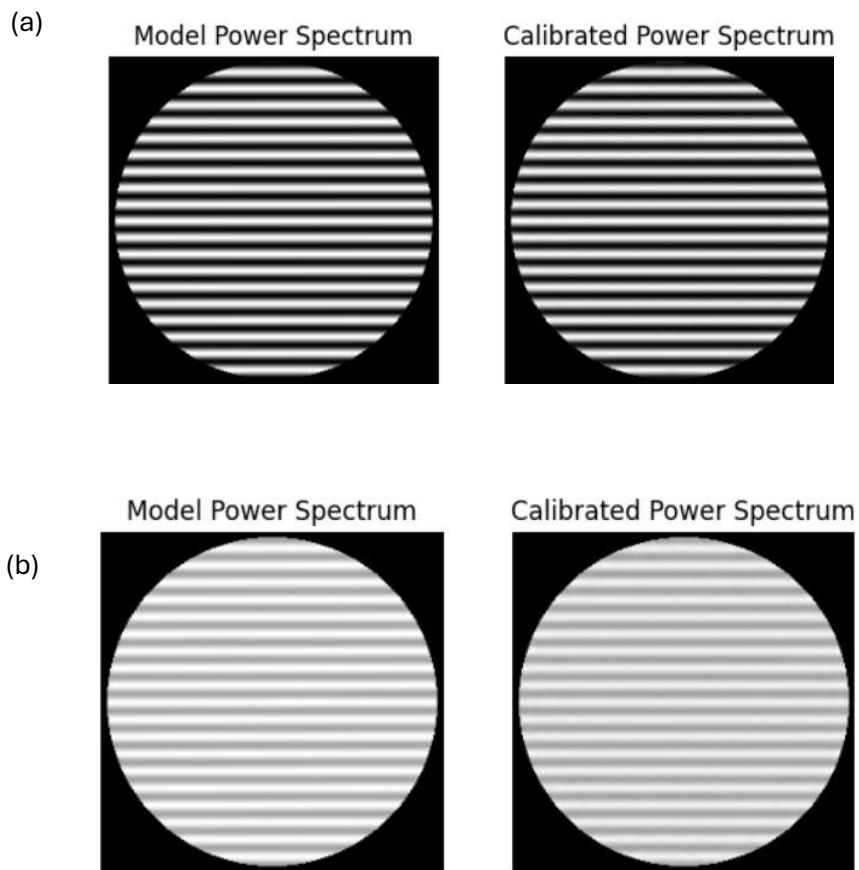


Figure 3.15: Model PS along with the calibrated PS. $\rho = 0.258''$, $\theta = 90^\circ$, $K = 1,500,000$. (a) $I = 1.0$, (b) $I = 0.1$.

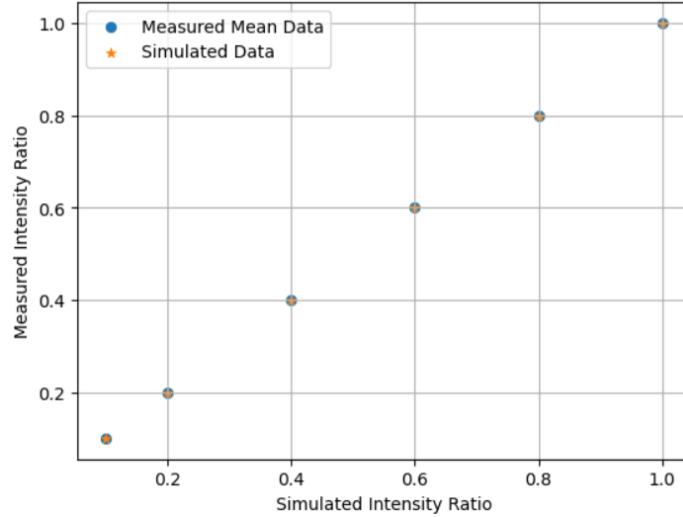


Figure 3.16: Recovered intensity ratios from the model under high photon condition. $\rho = 0.258''$, $\theta = 90^\circ$, $K = 1,500,000$

Table 3.4: Recovered separation and orientation from the model for simulation 3.1. Error shows the high accuracy of the model.

ρ (") (Simulated)	ρ (") (Measured)	θ (°) (Simulated)	θ (°) (Measured)	Average σ for Intensity
0.258	0.258	0.0	0.0	0.005964

- In all tested configurations, the recovered separations and position angles matched the simulated values exactly to three decimal places.
- The intensity ratio measurements exhibited very low variability, with mean $\sigma_{\text{Intensity}}$ values ranging from 0.0027 to 0.0080. This indicates a high degree of repeatability in the recovered intensity ratios.
- No degradation in accuracy was observed for small separations (e.g., 0.077" in Simulation 1.1) compared to larger separations (e.g., 0.258" in Simulation 1.3), suggesting robustness across the tested parameter space.
- The small uncertainties indicate that error bars on plotted results would be smaller than the marker size; therefore, in figures, a note will indicate that error bars are present but not visible at the scale used.
- The lowest limit for separation for accurate recovering of binary star parameters was 0.038". Smaller separations fall below the diffraction limit of the telescope.
- 0.1 was the lowest intensity ratio recoverable as below this, the fringe contrast was too weak for the algorithm to work.

The binary star parameter extraction algorithm demonstrated excellent accuracy in recovering separation, orientation, and intensity ratio for all tested configurations. The

recovered values were in exact agreement with the simulated inputs, with very small intensity uncertainties. This validates the robustness of the speckle interferometry model-fitting approach under high-photon-count conditions.

Subsequent sections will examine the performance of the algorithm under photon-limited conditions and with GLAO-corrected data.

3.4.2 Photon-Limited Conditions

To evaluate the performance of the parameter extraction algorithm under photon-limited conditions, the same binary configurations as described in section 3.4.1 were used, but the number of detected photoevents, K , was progressively reduced. Simulations were performed at $K=200,000$, $K = 25,000$ and the results were compared to the high-photon-count case ($K=1,500,000$). The reference star will also receive the same number of photoevents.

Simulation 2.1: $\rho = 0.077''$, $\theta = 270.0^\circ$

$K = 200,000$:

Below is an example of a calibrated PS:

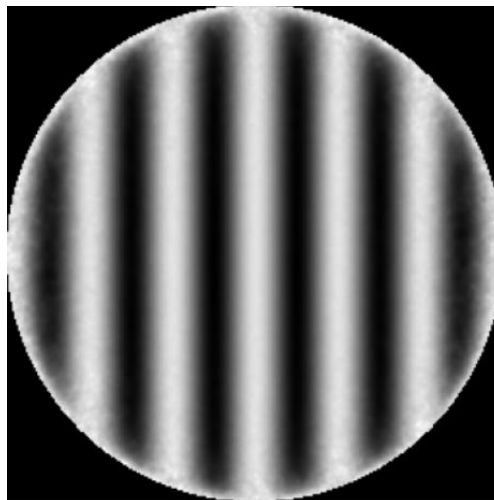


Figure 3.17: Calibrated PS, $\rho = 0.077''$, $\theta = 270^\circ$, $I = 1.0$, $K = 200,000$.

At 200,000 detected photoevents, the calibrated power spectrum shows degradation at its edges compared to the high-photon case. This effect was more apparent in the corresponding power spectrum SNR, where many high spatial frequencies fall below the threshold value of unity. Since the algorithm only uses frequencies with $\text{SNR} \geq 1$, these frequencies were excluded from the fitting process.

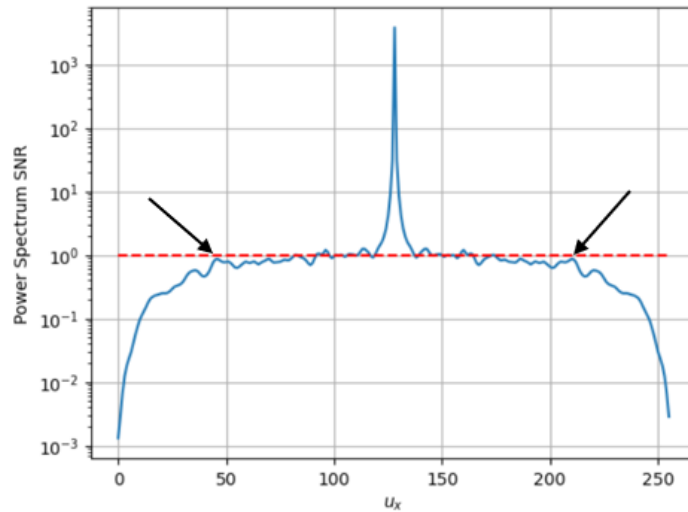


Figure 3.18: Power spectrum SNR for a reference star. $K = 200,000$

An example of a result from the model is shown below:

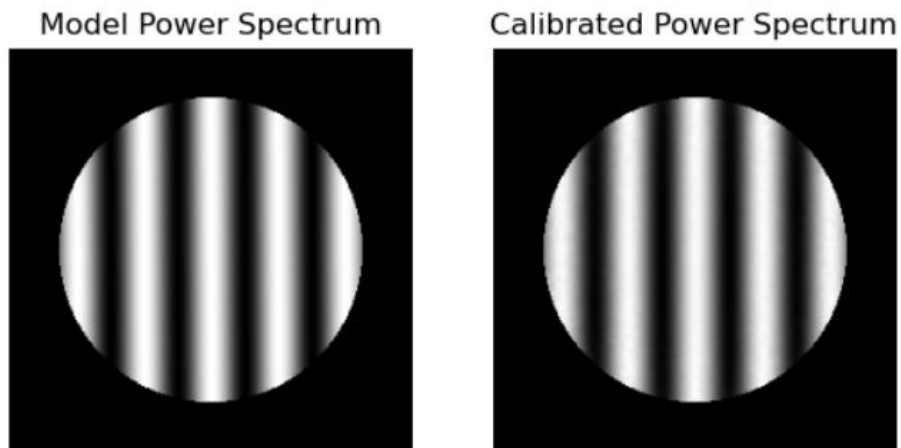


Figure 3.19: Model PS along with the calibrated PS. $\rho = 0.077''$, $\theta = 270^\circ$, $K = 200,000$. (a) $I = 1.0$, (b) $I = 0.1$.

Figure 3.19 shows that several spatial frequencies were removed corresponding to Figure 3.18 where the SNR drops significantly below one.

The results for the different intensities for this configuration are shown below;

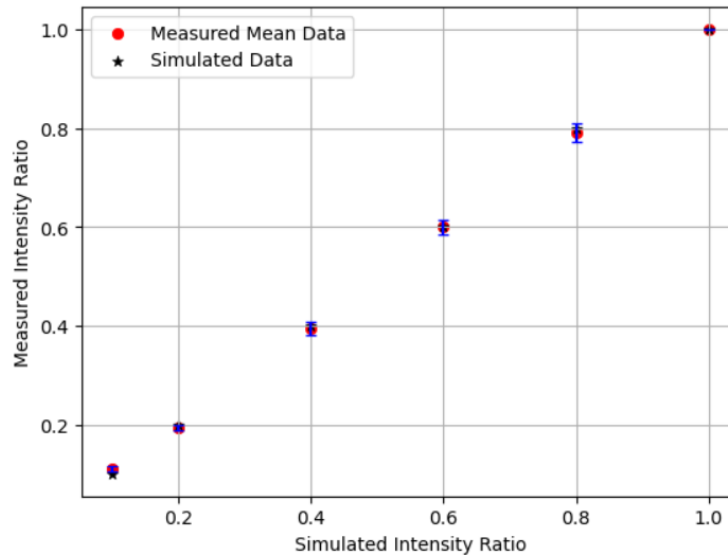


Figure 3.20: Recovered intensity ratios from the model under limited photon condition. $p = 0.077''$, $\theta = 270^\circ$, $K = 200,000$. Error bars denote the standard deviation of the recovered intensity ratios over ten independent simulations.

Unless otherwise stated, error bars in all figures represent the standard deviation of the recovered intensity ratio values across 10 independent simulations. Although the reduction in available spatial frequencies decreases the effective data set, the algorithm was still able to recover the binary parameters accurately. However, an increase in uncertainty was observed in the intensity ratio, particularly near parity (intensity ratio ≈ 0.8). This reflects the diminished contrast in the fringes of the power spectrum.

K = 25,000:

Here is an example of a calibrated PS with an intensity of 1.0 and 25,000 photoevents detected

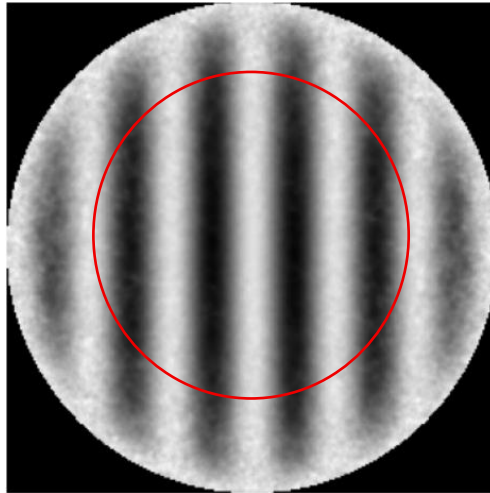


Figure 3.21: Calibrated PS, $\rho = 0.077''$, $\theta = 270^\circ$, $I = 1.0$, $K = 25,000$.

At 25,000 detected photoevents, the degradation in the calibrated power spectrum becomes severe. The contrast of the fringes was significantly reduced, leading to a detrimental impact on parameter extraction. The corresponding SNR plot shows that only a very limited number of spatial frequencies exceed the unity threshold.

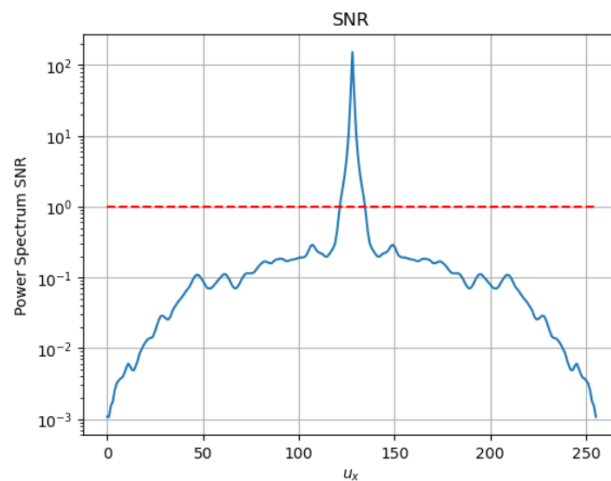


Figure 3.22: Power spectrum SNR for a reference star. $K = 25,000$.

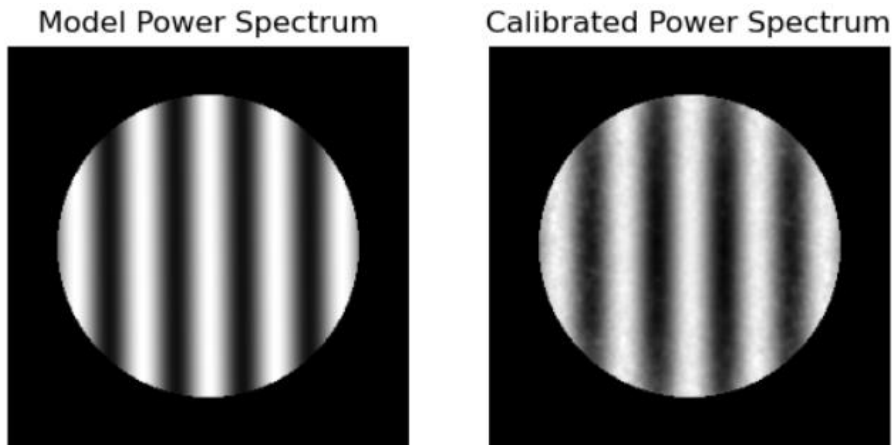


Figure 3.23: Model PS along with the calibrated PS. $\rho = 0.077''$, $\theta = 270^\circ$, $K = 25,000$. (a) $I = 1.0$, (b) 0.1 .

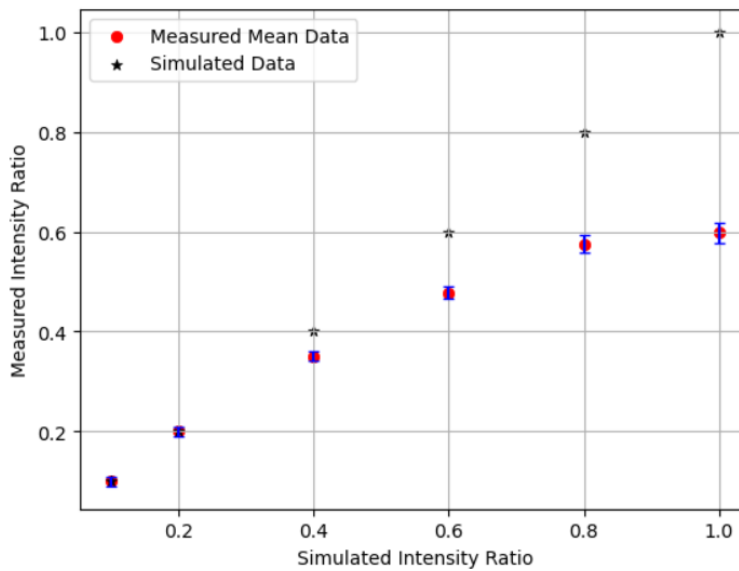


Figure 3.24: Recovered intensity ratios from the model under limited photon condition. $\rho = 0.077''$, $\theta = 270^\circ$, $K = 25,000$.

In practice, the algorithm was forced to retain frequencies of approximately where there is good fringe contrast, even if their SNR was below unity, in order to extract meaningful results. Despite this adjustment, the accuracy of the recovered parameters declined noticeably, with intensity ratios showing larger deviations from their simulated values. The degradation was most pronounced for binary systems with near-equal intensities, as the loss of fringe contrast makes the algorithm biased to a lower intensity ratio estimate.

Table 3.5: Error % from recovered intensity ratio for both photon levels. $\rho = 0.077''$, $\theta = 270^\circ$

K	Error % $I_{1.0}$	Error % $I_{0.8}$	Error $I_{0.6}$	Error % $I_{0.4}$	Error % $I_{0.2}$	Error % $I_{0.1}$
200,000	4.9	0.4	0.3	0.5	0.5	1.0
25,000	40.2	28.13	20.33	12.50	5.21	3.33

Full figure sets are shown for a representative case; for the remaining simulations, only tabulated results are presented, as the trends were consistent.

Simulation 2.2: $\rho = 0.179''$, $\theta = 59.74^\circ$

Following the same process outlined above, here the results for simulation 2.2:

Table 3.6: Recovered intensity ratios for both photon levels. $\rho = 0.179''$, $\theta = 59.74^\circ$.

	K = 200,000	K = 25,000
$I_{\text{Simulated}}$	I_{measured}	I_{measured}
1.0	1.0 ± 0	0.74 ± 0.032
0.8	0.79 ± 0.03	0.72 ± 0.022
0.6	0.60 ± 0.014	0.58 ± 0.034
0.4	0.4 ± 0.014	0.39 ± 0.022
0.2	0.19 ± 0.005	0.2 ± 0.021
0.1	0.11 ± 0.006	0.11 ± 0.00

Table 3.7: Error % from recovered intensity ratio for both photon levels. $\rho = 0.179''$, $\theta = 59.74^\circ$.

K	Error % $I_{1.0}$	Error % $I_{0.8}$	Error % $I_{0.6}$	Error % $I_{0.4}$	Error % $I_{0.2}$	Error % $I_{0.1}$
200,000	0	1.25	0	1.25	3.33	10.0
25,000	25.83	10.63	3.33	3.33	1.07	0.75

Simulation 2.3: $\rho = 0.219''$, $\theta = 45.0^\circ$

*Table 3.8: Recovered intensity ratios for both photon levels.
 $\rho = 0.219''$, $\theta = 45^\circ$.*

	K = 200,000	K = 25,000
$I_{\text{Simulated}}$	I_{measured}	I_{measured}
1.0	1.0 ± 0.02	0.8 ± 0.026
0.8	0.79 ± 0.03	0.73 ± 0.27
0.6	0.60 ± 0.01	0.59 ± 0.012
0.4	0.4 ± 0.01	0.40 ± 0.005
0.2	0.18 ± 0.00	0.20 ± 0.01
0.1	0.09 ± 0.01	0.10 ± 0.00

Table 3.9: Error % from recovered intensity ratio for both photon levels. $\rho = 0.219''$, $\theta = 45^\circ$.

K	Error % $I_{1.0}$	Error % $I_{0.8}$	Error % $I_{0.6}$	Error % $I_{0.4}$	Error % $I_{0.2}$	Error % $I_{0.1}$
200,000	0.0	1.88	0.0	1.25	3.33	1.67
25,000	20.0	8.74	1.67	1.02	0.87	0.03

Simulation 2.4: $\rho = 0.258''$, $\theta = 9.0^\circ$

Table 3.10: Recovered intensity ratios for both photon levels. $\rho = 0.258''$, $\theta = 90^\circ$.

	K = 200,000	K = 25,000
$I_{\text{Simulated}}$	I_{measured}	I_{measured}
1.0	1.0 ± 0.0	0.82 ± 0.038
0.8	0.80 ± 0.05	0.72 ± 0.033
0.6	0.61 ± 0.03	0.59 ± 0.026
0.4	0.4 ± 0.01	0.39 ± 0.01
0.2	0.2 ± 0.00	0.20 ± 0.01
0.1	0.10 ± 0.01	0.10 ± 0.00

Table 3.11: Error % from recovered intensity ratio for both photon levels. $\rho = 0.258''$, $\theta = 90^\circ$.

K	Error % $I_{1.0}$	Error % $I_{0.8}$	Error % $I_{0.6}$	Error % $I_{0.4}$	Error % $I_{0.2}$	Error % $I_{0.1}$
200,000	0.0	0.63	1.11	1.25	1.67	1.83
25,000	19.40	10.00	1.67	2.50	1.97	1.67

The photon-limited simulations demonstrate the strong dependence on the number of photons detected and the recovery of the intensity ratio of the binary. At high photon counts ($K=200,000$), the algorithm consistently recovered binary parameters with high accuracy: separations and orientations matched the simulated values, and intensity ratios were measured within a few percent of their true values.

As photon counts were reduced, systematic degradation became apparent. At $K=25,000$, fringe contrast in the calibrated power spectrum was significantly reduced, and many high-frequency components fell below the SNR threshold. This resulted in systematic underestimation of the measured intensities, particularly at high intensity ratios ($I \approx 1.0$), where errors exceeded 20%. This deviation was caused by the loss of high-frequency fringes in the power spectrum under atmospheric turbulence, which reduces fringe contrast and biases the recovered intensities toward lower values. Although separation and orientation remained recoverable, the accuracy of intensity ratios declines.

One result of interest is the error in intensity vs separation. There's a clear increase in error as the separation between the binary decreases.

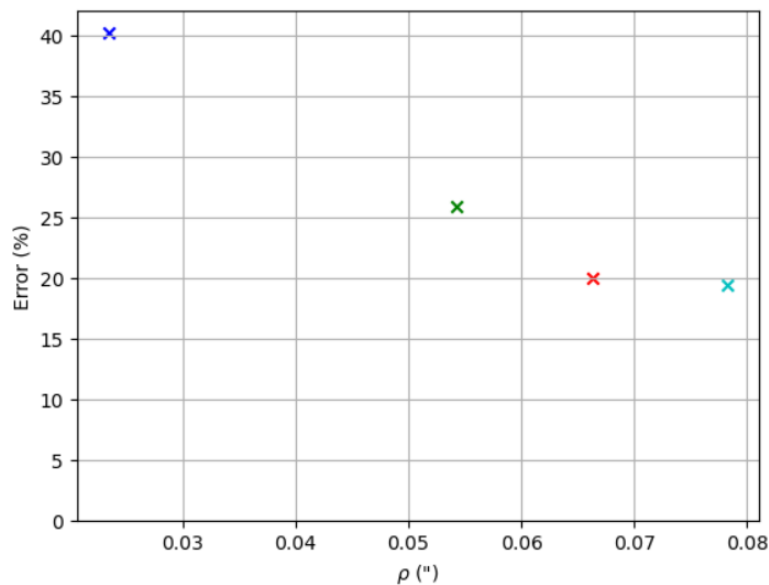


Figure 3.25: Error in intensity ratio for an intensity ratio of one. For all simulations, $K = 25,000$.

This trend can be explained by the figure below (Fig 3.26).

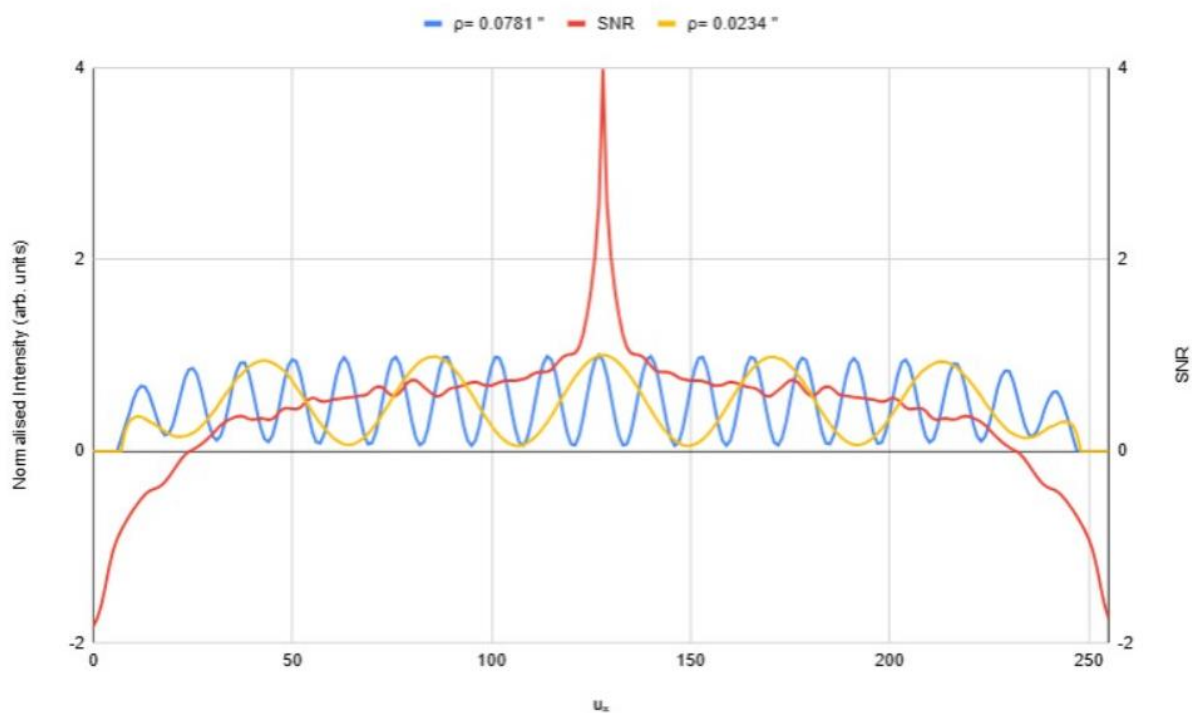


Figure 3.26: Comparison of frequency of fringes for different separations in relation to SNR. Each simulation, $K = 100,000$. The SNR is logarithmically scaled. These fringes are a 1D projection of their respective calibrated PS.

This figure shows that for the larger separation; more fringes fall within an area of higher SNR. This improves the accuracy of the recovered binary parameters. In contrast, for smaller separations fewer fringes fall within the high-SNR, leading to reduced sensitivity and larger errors in the estimated intensity ratio. Another aspect shown in figure 3.26 is that at the higher spatial frequencies for both binaries, the amplitude decreases, this was because of the degradation of the fringes due to limited photoevents.

Special case:

Simulations thus far have assumed the reference star has detected the same number of photoevents as the binary star. Using the same configuration as simulation 2.1 (simulation with most bias), but the reference star detected 1,000,000 photoevents results in figure below (Fig 3.27)

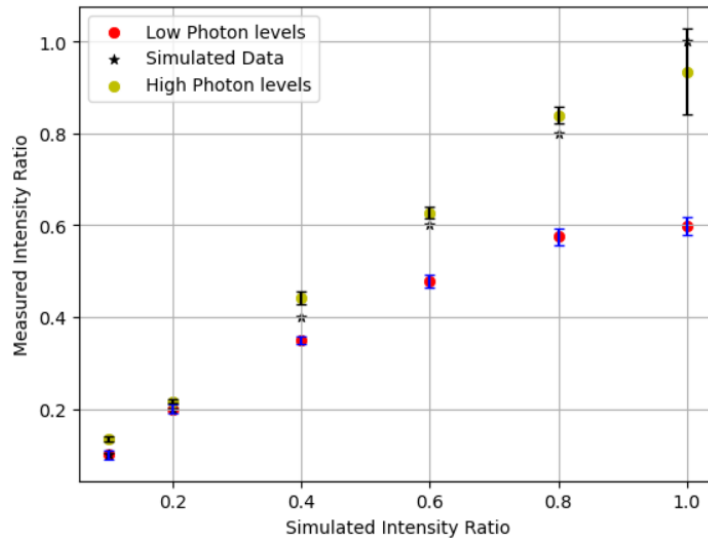


Figure 3.27: Measured Intensity ratios for when high and low levels of photons detected for the reference star. $p = 0.077''$, $\theta = 270^\circ$. Red dot $K = 25,000$, yellow dot $K = 1,000,000$.

When high photoevents were detected in the reference star, the severity of the bias for high intensity ratio binaries decreased. This bias stems from the division by the reference PS on the binary PS. The same results were seen across the other simulations. However, due to the unlikelihood of having a bright reference star near the test binary star, the subsequent section, will deal with the reference star detecting the same number of photons as the binary star.

3.4.3 GLAO Results

Using the adaptive optics system described in section 2.7, the results for GLAO corrected data are presented below.

Figure 3.27 illustrates the visual effect of the removal 120 Zernike modes from the perturbed wavefront. The uncorrected image shows strong distortion from atmospheric turbulence, with the binary components convolved with random speckle. After correction the image approaches the diffraction-limited case, with the two stars more clearly resolved. For this simulation, there was only one phase screen used, this was to highlight the ability of removing Zernikes modes from an atmospherically perturbed wavefront.

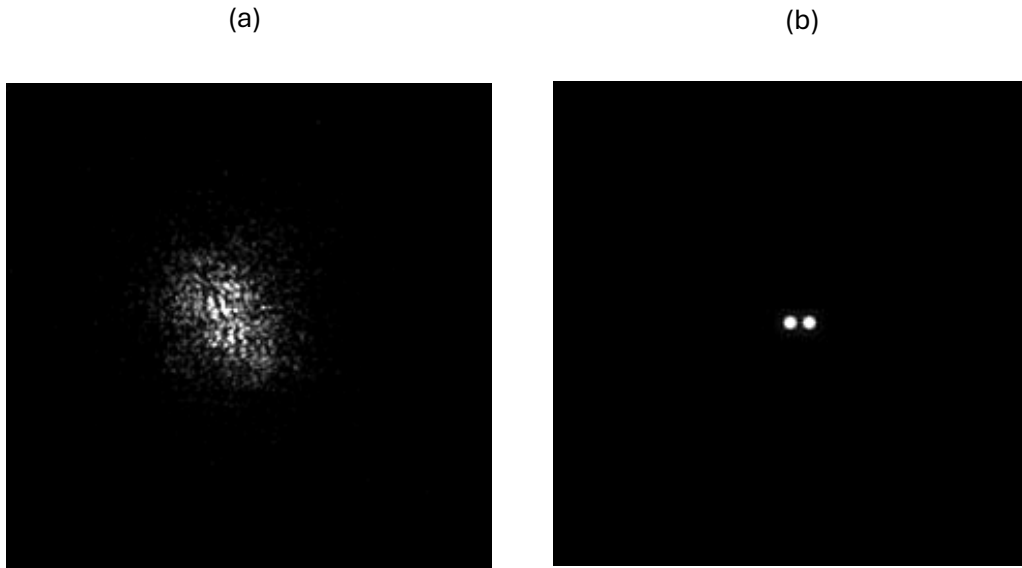


Figure 3.28: (a) Uncorrected speckle image. (b) Corrected speckle. $\rho = 0.077''$, $\theta = 270^\circ$, $I = 1.0$, $K = 100,000$. Fig 3.28 (b) dimensions are 128x128 pixels. This was done to make it easier for the reader to see the binary stars.

The following simulation resumes the same configuration as tested in high and low light level conditions (two phase screens). Figure 3.28 shows the comparison from an uncorrected speckle image and a corrected speckle image. Up to 120 Zernike modes were removed from the ground-layer phase screen.

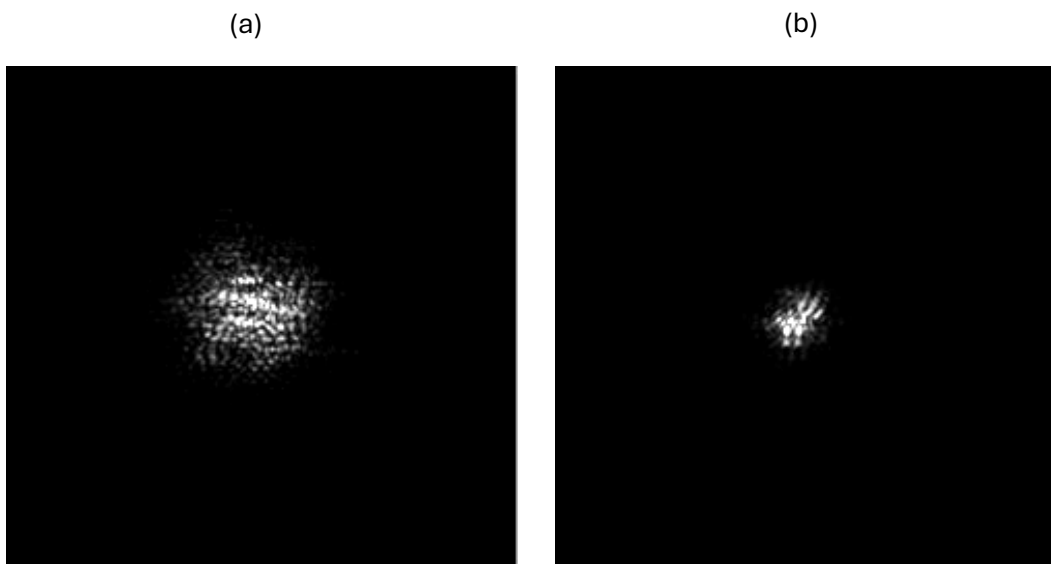


Figure 3.29: Visualisation of GLAO on a speckle image. (a) Uncorrected speckle image. (b) Corrected speckle image (up to 120 Zernikes modes were corrected). $\rho = 0.077''$, $\theta =$

It was clear that correcting the atmosphere reduces the number of speckles and concentrates them to their respective star. Figure 3.28 (b) and Figure 3.29 (b) shows an example of the difference between a classical AO system and GLAO system.

Figure 3.30 shows the effect of GLAO correction on the power spectrum SNR. Without correction, the SNR falls off with spatial frequency, and most high-frequency information was lost. After correction, the SNR improves, extending the range of usable frequencies.

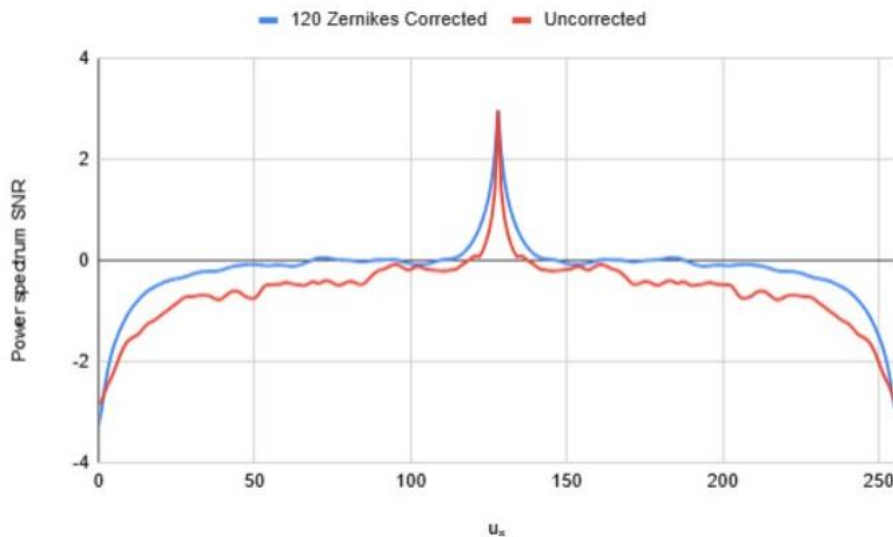


Figure 3.30: Power spectrum SNR for a reference star. $K = 100,000$. Up to 120 Zernikes modes were removed from the wavefront for the corrected SNR. SNR was logarithmically scaled.

Adding GLAO to the results from the photon limited conditions above are presented below.

Simulation 3.1: $\rho = 0.077''$, $\theta = 270.0^\circ$

Following the same procedure for photon limited conditions with the removal of Zernike modes.

K = 50,000

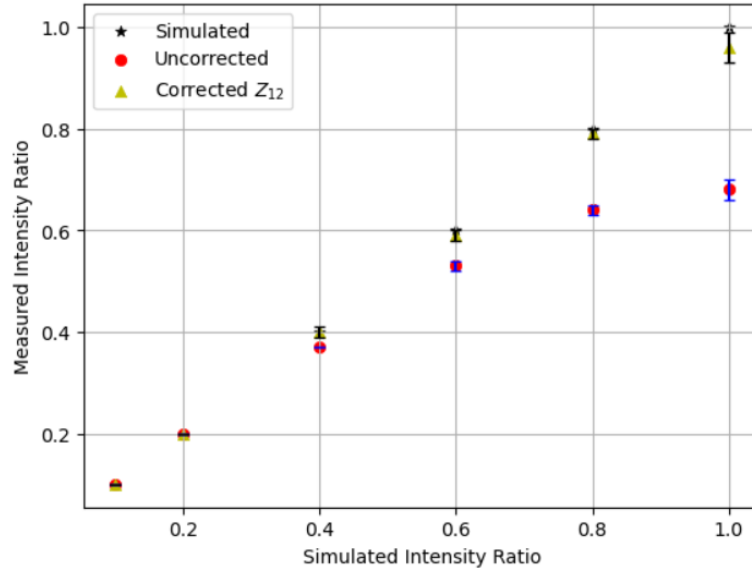


Figure 3.31: Recovered intensity ratios from the model under limited photon condition and GLAO corrected conditions. $\rho = 0.077''$, $\theta = 270^\circ$, $K = 50,000$

Figure 3.31 shows that correcting up to 12 Zernike modes of the aberrations from the atmosphere, the model was able to recover all the intensities to within an error of <5%. With GLAO correction (orange triangles), the recovered intensities follow the simulated values much more closely across the full range. At parity ($I=1.0$), the corrected case aligns almost exactly with the true input, whereas the uncorrected case still falls short. At intermediate values (e.g., $I=0.6-0.8$), GLAO correction also reduces the bias, and the error bars remain small, demonstrating improved stability.

K = 25,000



Figure 3.32: Recovered intensity ratios from the model under limited photon condition and GLAO corrected conditions. $\rho = 0.077''$, $\theta = 270^\circ$, $K = 25,000$.

At $K = 25,000$, the removal of up to 60 Zernike modes was capable of recovering every intensity ratio correctly. This demonstrates that the more Zernike modes removed, the more accurate the algorithm.

These figures illustrate that GLAO correction significantly improves the fidelity of intensity ratio recovery under photon-limited conditions, reducing systematic biases that appear in the uncorrected case and ensuring that the measured values track the true simulated inputs more reliably.

Pushing the GLAO system to its limits results in the following graph.

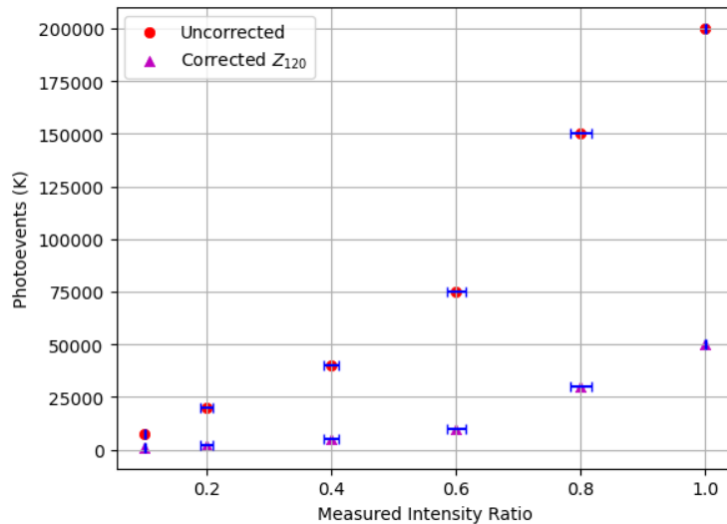


Figure 3.33: Minimum number of detected photoevents required for successful recovery of each intensity ratio. $p = 0.077''$, $\theta = 270^\circ$.

Figure 3.33 compares the minimum number of detected photoevents required for reliable binary parameter recovery as a function of the measured intensity ratio, both for the uncorrected case and with GLAO correction (120 Zernike modes removed). Each point represents when the error of the recovered mean intensity ratio was less than 5%.

In the uncorrected case (red markers), the required photoevents increases sharply as the intensity ratio approaches parity. For example, when both stars have equal brightness ($I=1.0$), more than 200,000 photoevents are required to achieve stable recovery. Even for moderate intensity ratios (e.g. $I=0.6$), the photon requirement remains above 75,000. This reflects the loss of fringe contrast in the power spectrum under uncorrected seeing conditions.

With GLAO correction (magenta markers), the photoevent requirement was reduced by more than an order of magnitude across all tested intensity ratios. At parity ($I=1.0$), stable recovery was possible with as few as $\sim 10,000$ photoevents. For fainter companions ($I=0.2$), the requirement falls to only a few hundred photoevents. This demonstrates that GLAO significantly improves the effective signal-to-noise ratio of the fringes, allowing reliable extraction of binary parameters under photon-limited conditions.

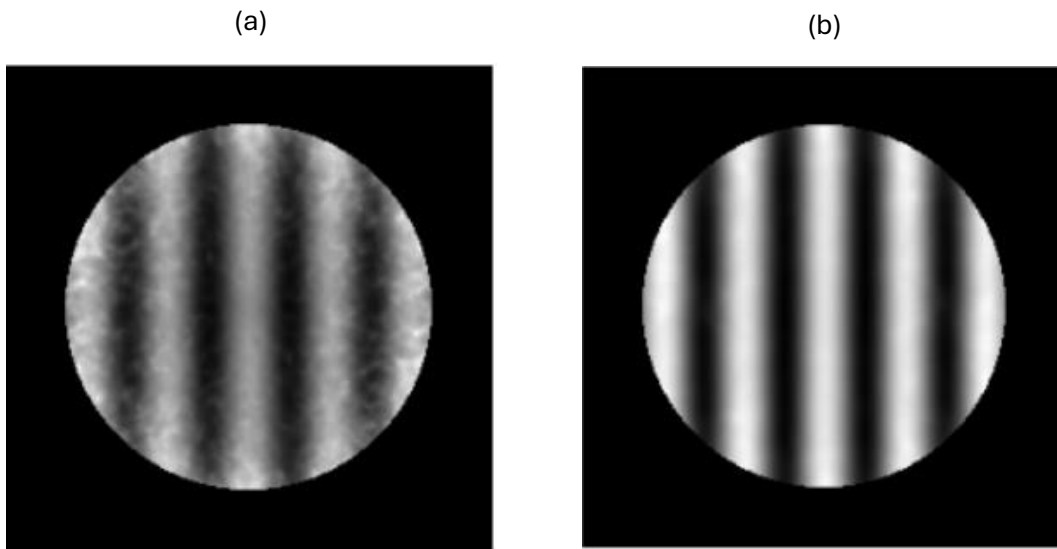


Figure 3.34: Comparison of a (a) uncorrected PS and (b) GLAO corrected calibrated PS. $\rho = 0.077''$, $\theta = 270^\circ$, $I = 1.0$, $K = 10,000$.

In the uncorrected spectrum, the fringes are significantly degraded by atmospheric turbulence. The noise dominates the image, and much of the high-frequency information was obscured. This loss of fringe visibility directly limits the accuracy of binary parameter recovery, particularly for intensity ratios, which depend on the contrast of these fringes.

By contrast, the fully corrected spectrum exhibits clear, high-contrast fringes that extend usable frequencies. The removal of low- and high-order aberrations concentrates the signal into deterministic fringes, effectively restoring the diffraction-limited information content despite the photon-limited regime.

Overall, these results highlight how GLAO correction extends the operational range of the algorithm, lowering the photon threshold required for successful parameter recovery.

Simulation 3.2: $\rho = 0.179''$, $\theta = 59.74^\circ$

$K = 25,000$

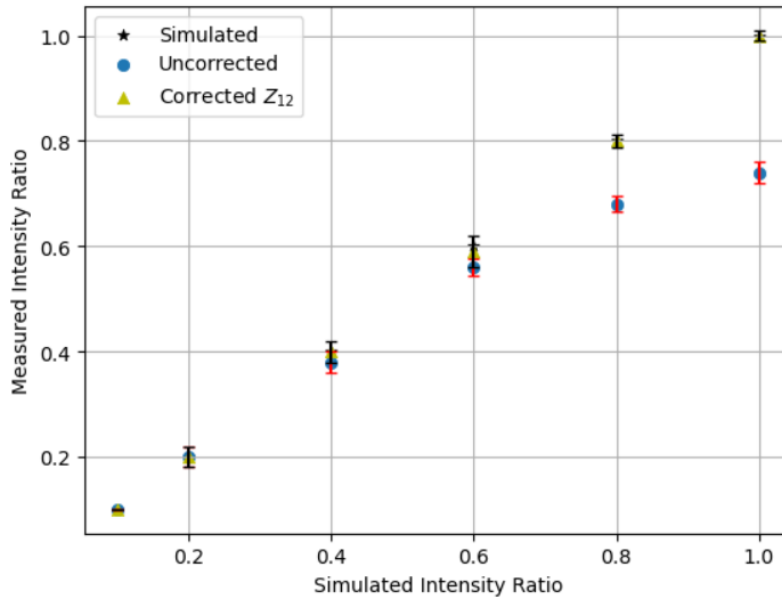


Figure 3.35: Recovered intensity ratios from the model under limited photon condition and GLAO corrected conditions. $\rho = 0.179''$, $\theta = 59.74^\circ$, $K = 25,000$.

Figure 3.35 outperforms the simulation 1.3 for the same reason explained in Figure 3.26.

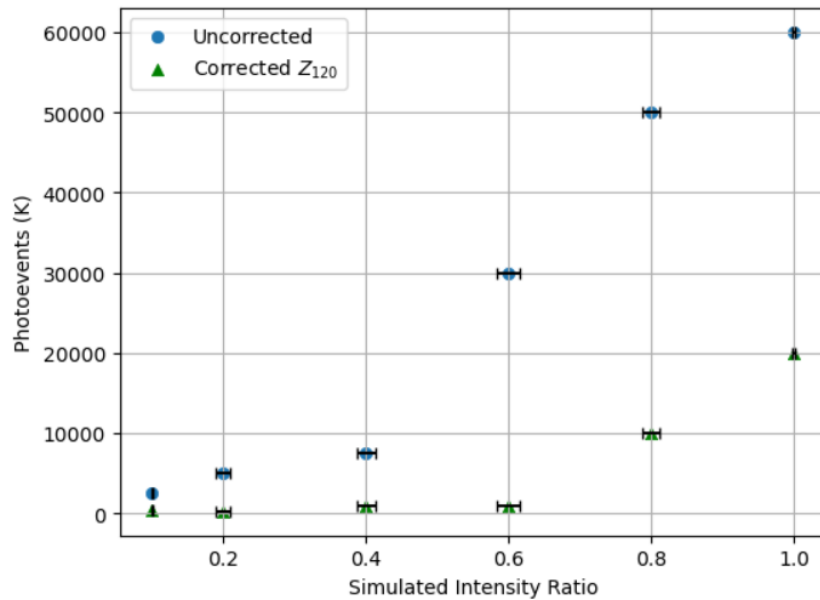


Figure 3.36: Minimum number of detected photoevents required for successful recovery of each intensity ratio. $\rho = 0.179''$, $\theta = 59.74^\circ$.

Simulation 3.3: $\rho = 0.219''$, $\theta = 45.0^\circ$

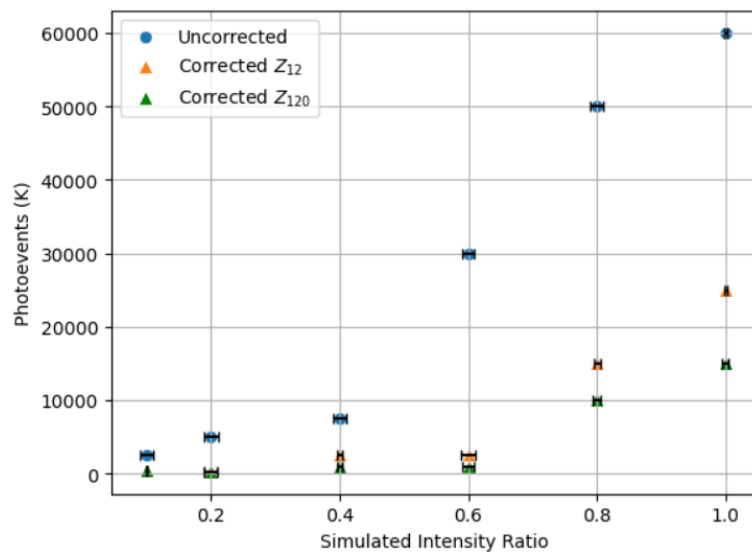


Figure 3.37: Minimum number of detected photoevents required for successful recovery of each intensity ratio. $\rho = 0.219''$, $\theta = 45^\circ$.

This graph shows the minimum number of photons required for two different degrees of correction, for the algorithm to recover the correct intensity ratio. It was seen that the removal of 12 Zernikes extends the algorithm's performance for intensity ratios near parity by roughly an order of magnitude less photons, while as intensity ratios decrease, the improvement becomes less noticeable. This also shows there was only a marginal gain from the removal of 12 Zernikes to 120 Zernikes.

Simulation 3.4: $\rho = 0.258''$, $\theta = 90.0^\circ$

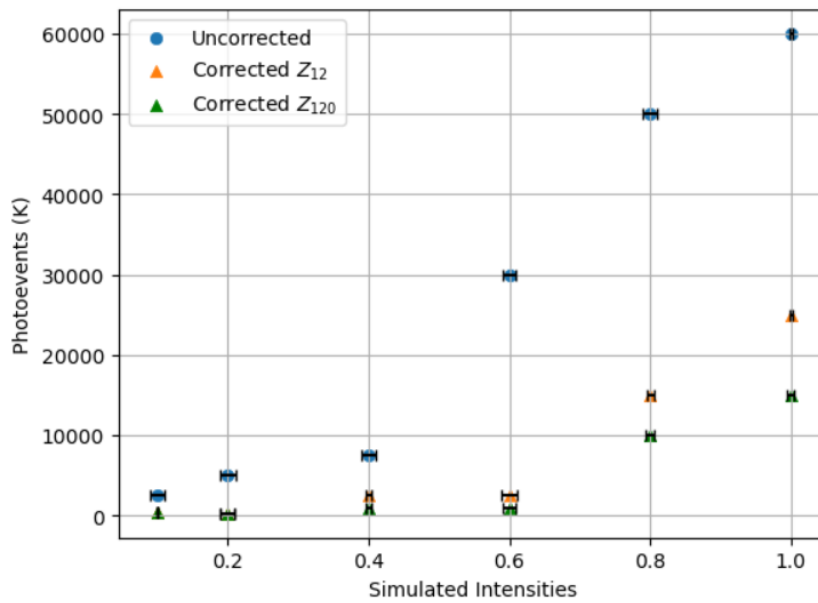


Figure 3.38: Minimum number of detected photoevents required for successful recovery of each intensity ratio. $\rho = 0.258''$, $\theta = 90^\circ$.

This simulation performed almost identically to simulation 4.3, showing the same trends.

3.4.4 Recovery of Fourier Phase

In this section we present the results that was detailed in section 2.5 and section 2.6 of the methodology.

The mean bispectrum of 1000 binary star speckle images was taken and a slice through the four-dimensional structure is shown in Figure 3.38.

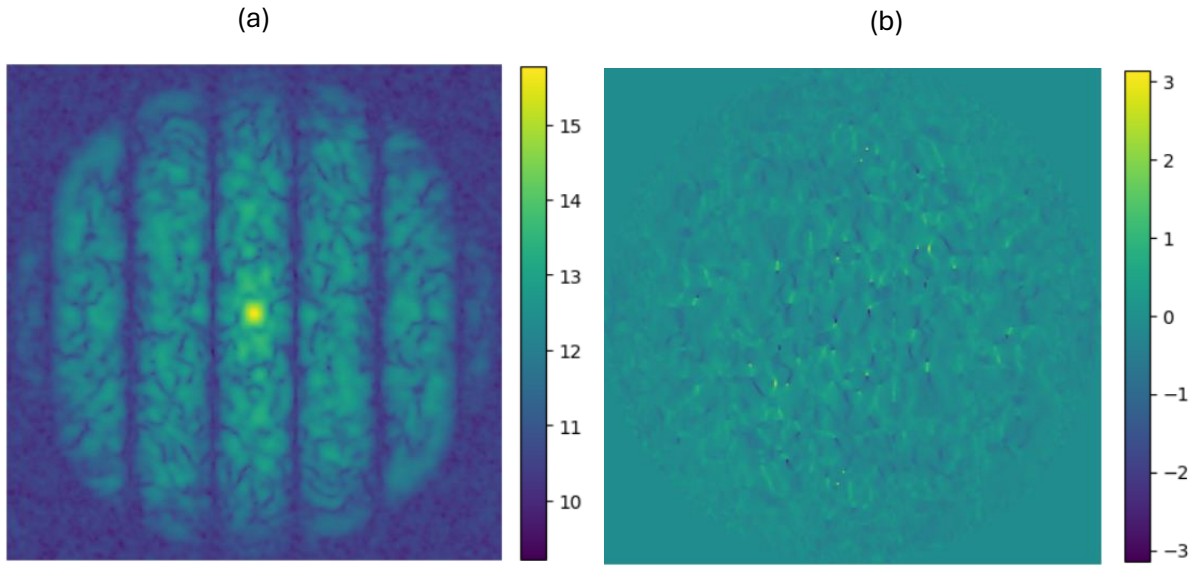


Figure 3.39: Mean bispectrum (a) modulus and (b) phase of binary star speckle images with configuration of $\rho = 0.077''$, $\theta = 270^\circ$, $K = 200,000$. Subplanes used for (a), $u_2 = 0$, $v_2 = 0$. Subplanes used for (b), $u_2 = 0$, $v_2 = 1$. The bispectrum modulus is logarithmically scaled.

The resulting bispectral SNR, calculated using Equation 2.23, for the mean bispectrum of the example presented in Figure 3.39, is shown in Figure 3.40.

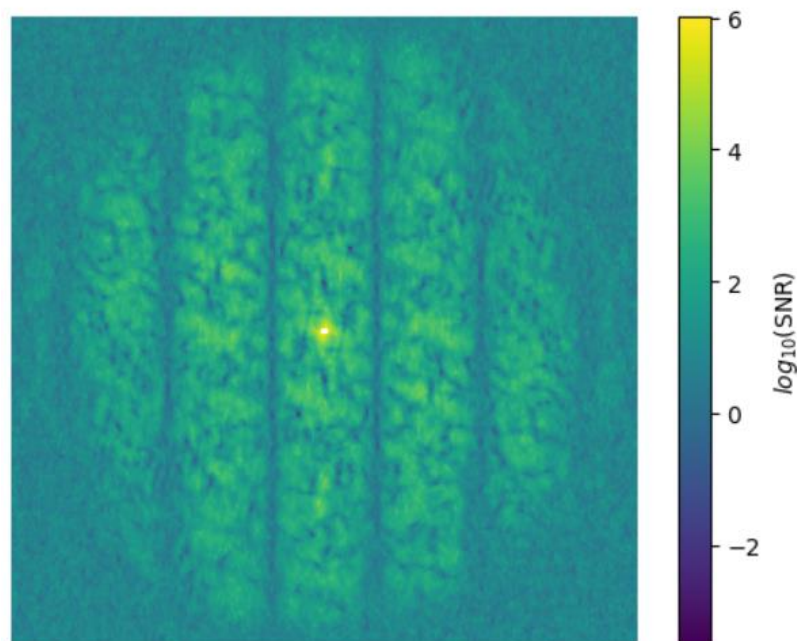


Figure 3.40: Logarithmic bispectral SNR. Subplanes used $u_2 = 0$, $v_2 = 1$.

This is the SNR used in the weighting for Equation 2.27.

The separation, ρ , and orientation, θ , was found from the ACF, however stated previously that there is an 180° ambiguity. The recovery of the Fourier phase using the model of Equation (2.25) and minimizing the cost function of Equation (2.27), the orientation of the binary star was found. Both orientations were used in the cost function, and whichever produced the smallest error was the correct orientation of the binary star. Each test used six subplanes from the bispectrum, which Glindemann, noted that it was enough to determine the orientation of the binary star with the least computation. The results are presented below.

Table 3.12: Error from cost function for high-light levels, across all simulated intensity ratios. $K = 200,000, \rho = 0.077$ "

Simulated Intensities	Error $\theta = 270^\circ$ (Correct)	Error $\theta = 90^\circ$
1.0	65872.35	66088.13
0.8	8035.62	27743.52
0.6	3507.52	29527.28
0.4	2678.69	10833.15
0.2	3234.29	5475.15
0.1	2709.86	3794.60

Table 3.13: Error from cost function for low-light levels across all simulated intensity ratios. $K = 25,000, \rho = 0.077$ "

Simulated Intensities	Error $\theta = 270^\circ$ (Correct)	Error $\theta = 90^\circ$
1.0	6109.77	6512.63
0.8	4540.52	7916.60
0.6	2860.97	7736.48
0.4	2001.84	5968.68
0.2	1733.76	3679.61
0.1	1947.02	2180.75

Table 3.14: Error from cost function for GLAO conditions, across all simulated intensity ratios. $K = 25,000$, $\rho = 0.077$ ". Up to 120 Zernike's was corrected.

Simulated Intensities	Error $\theta = 270^\circ$ (Correct)	Error $\theta = 90^\circ$
1.0	30061.51	32009.28
0.8	11484.25	36330.08
0.6	4302.42	32797.65
0.4	2084.25	30039.75
0.2	1198.47	7174.65
0.1	1052.59	2749.52

This showed that for high-light levels, low-light levels, and for GLAO corrected conditions, for all intensity ratios, the recovery of the Fourier phase was able to determine the orientation of the binary star. The same results were seen in the other simulations.

With this algorithm, all binary star parameters can now be successfully recovered.

Chapter 4 Discussion & Conclusion

This research investigated the limits and performance of speckle interferometry for recovering the physical parameters of binary star systems under realistic atmospheric conditions, using a fully simulated framework that incorporated Kolmogorov turbulence, photon-limited imaging, and ground-layer adaptive optics correction. By combining rigorous simulations with detailed Fourier analysis, the study provides a comprehensive assessment of both the capabilities and the practical constraints of speckle interferometry.

Summary of Findings

1. High Photon levels

High-photon-count simulations confirmed that the SI pipeline reliably recovered binary parameters (separation, position angle, and intensity ratio) with sub-percent error. The calibrated power spectrum retained spatial frequencies up to the diffraction limit, demonstrating that short-exposure speckle images preserve diffraction-limited information even when long-exposure images are dominated by a seeing disc.

2. Photon limited Behaviour

In photon limited conditions, it became clear that a bias was introduced for intensity ratios near one. This was very apparent for $K = 25,000$ and below. This was the result of the degradation of contrast in the power spectrum fringes, ultimately leading to an underestimation of the intensity ratio of the binary. For decreasing intensity ratios, the contrast between the fringes in the power spectrum was naturally smaller, as a result of this, there was a less pronounced bias. The algorithm was still able to recover intensity ratios of 0.1 and 0.2 with 1000 photoevents.

3. Ground-Layer Adaptive Optics Enhancement

Simulations incorporating GLAO, implemented as the removal of up to 120 Zernike modes, showed a dramatic extension of SI performance. GLAO improved fringe contrast across the power spectrum, reduced the photon requirement for full parameter recovery by more than an order of magnitude in some cases, and sharply decreased systematic underestimation of intensity ratios. These results underscore the value of GLAO correction for wide-field, visible-light binary studies.

4. Fourier Phase Recovery

A least-squares bispectrum algorithm successfully reconstructed the object's Fourier phase, resolving the intrinsic 180° position-angle ambiguity of the power-spectrum method. The phase recovery remained robust under both high- and moderate-photon regimes, validating the use of bispectrum analysis for unambiguous orientation measurements.

Future Work

Several avenues for further investigation arise from this study:

- **Application to Real Observations:** Applying real telescope data to this algorithm, will validate the simulation-based thresholds and reveal additional instrumental effects such as detector noise and calibration errors.
- **Comprehensive AO System:** Due to the limited timescale of this thesis, adaptive-optics correction was modelled by the simple removal of Zernike modes. A more sophisticated GLAO simulation, incorporating closed-loop control, realistic wavefront sensing, and temporal dynamics, would yield a more realistic representation of modern GLAO performance and allow a deeper assessment of its impact on speckle-interferometric parameter recovery.
- **Image Reconstruction:** The bispectral phase recovery algorithm used in this thesis was only able to recover the orientation of the binary star. A more complex Fourier phase recovery algorithm (such that used in Negrete-Regagnon [35]) would be able to reconstruct the image of the binary star.

In conclusion, this thesis provides a quantitatively framework for binary-star parameter recovery using speckle interferometry across a wide range of observing conditions. It establishes realistic photon-count limits, demonstrates the substantial benefits of GLAO correction, and confirms the robustness of bispectrum phase recovery.

Bibliography

1. Tatarskii, V.I. and Zavorotny, V.U., 1993. Atmospheric turbulence and the resolution limits of large ground-based telescopes: comment. *Journal of the Optical Society of America A*, 10(11), pp.2410-2414.
2. Kolmogorov, A.N., 1941. The local structure of turbulence in incompressible viscous fluid for very large Reynolds. *Numbers. In Dokl. Akad. Nauk SSSR*, 30, p.301.
3. Labeyrie A. Attainment of Diffraction Limited Resolution in Large Telescopes by Fourier Analysing Speckle Patterns in Star Images. *Astronomy and Astrophysics*. 1970;6(1):85-87.
4. Kuwamura, S., Ono, S., Miura, N., Tsumuraya, F., Sakamoto, M. and Baba, N., 2020. Error correction and evaluation in astronomical speckle interferometry with low-light CCD camera. *Optical Review*, 27(6), pp.498-520.
5. Fried, D.L., 1966. Optical resolution through a randomly inhomogeneous medium for very long and very short exposures. *Journal of the Optical Society of America*, 56(10), pp.1372-1379.
6. Labeyrie, A., Bonneau, D., Stachnik, R.V. and Gezari, D.Y., 1974. Speckle interferometry. III. High-resolution measurements of twelve close binary systems. *Astrophysical Journal*, vol. 194, p. L147, 194, p.L147.
7. Horch, E.P., Dinescu, D.I., Girard, T.M., Van Altena, W.F., López, C.E. and Franz, O.G., 1996. Speckle Interferometry of Southern Double Stars. I. First Results of the Yale-San Juan Speckle Interferometry Program. *Astronomical Journal* v. 111, p. 1681, 111, p.1681.
8. McAlister, H.A., Mason, B.D., Hartkopf, W.I. and Shara, M.M., 1993. ICCD speckle observations of binary stars. X-A further survey for duplicity among the bright stars. *Astronomical Journal (ISSN 0004-6256)*, vol. 106, no. 4, p. 1639-1655., 106, pp.1639-1655.
9. Strakhov, I.A., Safonov, B.S. and Cheryasov, D.V., 2023. Speckle interferometry with CMOS detector. *Astrophysical Bulletin*, 78(2), pp.234-258.
10. Hartkopf, W.I., Mason, B.D., McAlister, H.A., Turner, N.H., Barry, D.J., Franz, O.G. and Prieto, C.M., 1996. ICCD Speckle Observations of Binary Stars. XIII. Measurements During 1989-1994 From the Cerro Tololo 4 M Telescope. *Astronomical Journal* v. 111, p. 936, 111, p.936.
11. Horch, E.P., Howell, S.B., Everett, M.E. and Ciardi, D.R., 2012. Observations of binary stars with the differential speckle survey instrument. IV. Observations of kepler, CoRoT, and hipparcos stars from the gemini north telescope. *The Astronomical Journal*, 144(6), p.165.
12. Horch, E., Ninkov, Z. and Franz, O.G., 2001. CCD Speckle Observations of Binary Stars from the Southern Hemisphere. III. Differential Photometry. *The Astronomical Journal*, 121(3), p.1583.
13. Tokovinin, A., 2018. Ten years of speckle interferometry at SOAR. *Publications of the Astronomical Society of the Pacific*, 130(985), p.035002.

14. Horch, E.P., Casetti-Dinescu, D.I., Camarata, M.A., Bidarian, A., van Altena, W.F., Sherry, W.H., Everett, M.E., Howell, S.B., Ciardi, D.R., Henry, T.J. and Nusdeo, D.A., 2017. Observations of binary stars with the differential speckle survey instrument. VII. Measures from 2010 September to 2012 February at the WIYN telescope. *The Astronomical Journal*, 153(5), p.212.
15. Roggemann, M.C. and Welsh, B.M., 2018. *Imaging through turbulence*. CRC press.
16. Lohmann, A.W., Weigelt, G. and Wirtitzer, B., 1983. Speckle masking in astronomy: triple correlation theory and applications. *Applied Optics*, 22(24), pp.4028-4037.
17. Ayers, G.R., Northcott, M.J. and Dainty, J.C., 1988. Knox–Thompson and triple-correlation imaging through atmospheric turbulence. *Journal of the Optical Society of America A*, 5(7), pp.963-985.
18. Glindemann, A., Lane, R.G., Dainty, J.C., Cappellini, V. and Constantinides, A.G., 1991. Least squares reconstruction of the object phase from the bispectrum. *Digital Signal Processing—91*, pp.59-65.
19. Marron, J.C., Sanchez, P.P. and Sullivan, R.C., 1990. Unwrapping algorithm for least-squares phase recovery from the modulo 2π bispectrum phase. *Journal of the Optical Society of America A*, 7(1), pp.14-20.
20. Northcott, M.J., Ayers, G.R. and Dainty, J.C., 1988. Algorithms for image reconstruction from photon-limited data using the triple correlation. *Journal of the Optical Society of America A*, 5(7), pp.986-992.
21. Babcock, H.W., 1953. The possibility of compensating astronomical seeing. *Publications of the Astronomical Society of the Pacific*, 65(386), pp.229-236.
22. Hippler, S., 2019. Adaptive optics for extremely large telescopes. *Journal of Astronomical Instrumentation*, 8(02), p.1950001.
23. Alan Mullen and Claudia Florinda, 2020. What Problem Does Adaptive Optics Correct?, <https://andor.oxinst.com/learning/view/article/adaptive-optics-correcting-distortions-to-enhance-resolution>, [Accessed 04 March 2025].
24. Tokovinin, A., Baumont, S. and Vasquez, J., 2003. Statistics of turbulence profile at Cerro Tololo. *Monthly Notices of the Royal Astronomical Society*, 340(1), pp.52-58.
25. Hart, M., Milton, N.M., Baranec, C., Powell, K., Stalcup, T., McCarthy, D., Kulesa, C. and Bendek, E., 2010. A ground-layer adaptive optics system with multiple laser guide stars. *Nature*, 466(7307), pp.727-729.
26. Tokovinin, A., 2004. Seeing improvement with ground-layer adaptive optics. *Publications of the Astronomical Society of the Pacific*, 116(824), p.941.
27. Quirrenbach, A., 2006. The effects of atmospheric turbulence on astronomical observations. *A. Extrasolar planets. Saas-Fee Advanced Course*, 31(137), p.137.
28. McLean, I.S., 2008. *Electronic imaging in astronomy: detectors and instrumentation* (Vol. 552). Berlin: Springer.
29. Townson, M.J., Farley, O.J.D., Orban De Xivry, G., Osborn, J. and Reeves, A.P., 2019. AOtools: a Python package for adaptive optics modelling and analysis. *Optics express*, 27(22), pp.31316-31329.
30. Schmidt, J.D., 2010. Numerical simulation of optical wave propagation with examples in MATLAB. *(No Title)*.

31. Assémat, F., Wilson, R.W. and Gendron, E., 2006. Method for simulating infinitely long and non stationary phase screens with optimized memory storage. *Optics express*, 14(3), pp.988-999.
32. Virtanen, P. et al., 2020. SciPy 1.0: Fundamental Algorithms for Scientific Computing in Python. *Nature Methods*, 17(3), pp.261–272. Available at: <https://docs.scipy.org/doc/scipy/> [Accessed 10 June 2025].
33. Levenberg, K., 1944. A method for the solution of certain non-linear problems in least squares. *Quarterly of applied mathematics*, 2(2), pp.164-168.
34. Andrew Dennis, 2018, What are adaptive optics?, <https://andor.oxinst.com/learning/view/article/introduction-to-adaptive-optics>, [Accessed 15 June 2025].
35. Negrete-Regagnon, P., 1996. Practical aspects of image recovery by means of the bispectrum. *Journal of the Optical Society of America A*, 13(7), pp.1557-1576.
36. Dainty, J.C. and Greenaway, A.H., 1979. Estimation of spatial power spectra in speckle interferometry. *Journal of the Optical Society of America*, 69(5), pp.786-790.
37. Wirnitzer, B., 1985. Bispectral analysis at low light levels and astronomical speckle masking. *Journal of the Optical Society of America A*, 2(1), pp.14-21.
38. Glindemann, A., Lane, R.G. and Dainty, J.C., 1992. Estimation of binary star parameters by model fitting the bispectrum phase. *Journal of the Optical Society of America A*, 9(4), pp.543-548.
39. Noll, R.J., 1976. Zernike polynomials and atmospheric turbulence. *Journal of the Optical Society of America*, 66(3), pp.207-211.
40. Roddier, N.A., 1990. Atmospheric wavefront simulation using Zernike polynomials. *Optical engineering*, 29(10), pp.1174-1180.
41. Thomas, S., 2004, October. A simple turbulence simulator for adaptive optics. In *Proc. SPIE* (Vol. 5490, pp. 766-773).